Cement and Concrete Composites 170 (2026) 106596

Contents lists available at ScienceDirect

Cement and Concrete Composites

journal homepage: www.elsevier.com/locate/cemconcomp

Study on the carbonization coating treatment of municipal solid waste incineration fine bottom ash as aggregates: CO_2 capture, contaminants solidification, on-site application scale

Helong Song [a,b,c], Zhihan Jiang [d], Theun S. Luinenburg [d], Florent Gauvin [d], Xiaowen Fu [e], Xiaohui Sun [a,b,c,*], Zijun Dong [a,b,c], Feng Wang [a,b,c], Huiming Fan [e], Xiangsheng Chen [a,b,c], H.J.H. Brouwers [d]

[a] Key Laboratory of Coastal Urban Soil-Water Environmental Evolution, Ministry of Ecology and Environment (under construction), Shenzhen University, Shenzhen, 518060, China
[b] State Key Laboratory of Intelligent Geotechnics and Tunnelling, Shenzhen University, Shenzhen, 518060, China
[c] College of Civil and Transportation Engineering, the Underground Polis Academy, Shenzhen University, Shenzhen, 518060, China
[d] Department of the Built Environment, Eindhoven University of Technology, P. O. Box 513, 5600 MB, Eindhoven, the Netherlands
[e] State Key Laboratory of Pulp and Paper Engineering, South China University of Technology, Guangzhou, 510641, China

ARTICLE INFO

Keywords:
MSWI bottom ash
Carbonation coating treatment
Core-shell structure
Leaching behaviour
Sustainability evaluation

ABSTRACT

The current carbonation technology of municipal solid waste incineration bottom ash (IBA) as aggregates has disadvantages such as low carbon capture efficiency, partial contaminant immobilization, and poor economic feasibility. Herein, a carbonation coating technology is proposed, where a $CaCO_3$@IBA core-shell structure is innovatively designed, accompanied by the generation of high-value byproduct precipitated calcium carbonate (PCC). This technology improves CO_2 sequestration content, reaching 246.45 mg CO_2/g IBA through strengthened mass transfer kinetics during aqueous carbonation reaction. Leaching behaviour tests and molecular dynamics simulation indicate that such a core-shell design facilitates the immobilization of different contaminants in IBA, achieving 49% for Cu, 90% for Zn, and 30% for Cl. When applied to cementitious composites, the composites exhibit a significant increase in mechanical strength, above 16% at a replacement level of 30%, compared to the IBA. Finally, based on geography-guided industrial-scale design, a projected net revenue of €32.9 million is achieved assuming 10 years of operating. This work establishes an innovative paradigm for synergistic IBA utilization, carbonation capture, and production of eco-friendly building aggregate and high-value byproduct PCC.

1. Introduction

With rapid urbanization and population growth, the generation of municipal solid waste (MSW) has dramatically increased in recent decades, bringing extensive public awareness of environmental issues [1,2]. As a typical by-product of modern urban lifestyle, MSW has reached an annual global production of approximately 2.01 billion tons and is projected to rise to 3.4 billion tonnes by 2050 [3]. This leads to great pressure on waste management.

Incineration technology, with the advantages of volume and weight reduction as well as detoxification and energy recovery, is widely adopted to manage MSW [4,5]. However, this treatment mainly generates two types of solid residues: fly ash and bottom ash. With the latter accounting for around 80% % by weight of the total incineration residues [6]. In Europe alone, about 20 million tons of municipal solid waste incineration bottom ash (IBA) are generated annually [7,8]. Conventionally, IBA is either disposed of in landfills or utilized as a secondary construction aggregate, substituting natural aggregates [9–13]. The former treatment not only wastes its potential reuse value but also consumes land resources. In contrast, the latter management option of construction material utilization is accepted as a promising recycling pathway of IBA [14–16]. Unfortunately, the leaching risk of contaminant ions (e.g., trace heavy metals, Cl^-, and SO_4^{2-}) severely constrain its large-scale application of IBA as a sand aggregate substitute

* Corresponding author. College of Civil and Transportation Engineering, Shenzhen University, Shenzhen, 518060, China
E-mail address: sunxiaohui@szu.edu.cn (X. Sun).

https://doi.org/10.1016/j.cemconcomp.2026.106596
Received 17 January 2026; Received in revised form 26 February 2026; Accepted 24 March 2026
Available online 26 March 2026

in the building sector [6,17]. When IBA is directly incorporated as a sand aggregate substitute, cementitious products such as C-S-H and C-A-S-H can partially immobilize contaminants present in IBA [10,18–20]; however, the presence of soluble salts, particularly chloride and sulfates, adversely affects the durability and mechanical strength of the resulting composites [21]. Particularly, fine IBA may still pose significant leaching risks even within the cementitious matrix [22]. Thus, alternative treatments before natural aggregate substitution, including water washing [23,24], acid/alkaline washing [25,26], and the use of organic chemical agents [27], have also been explored for the stabilization and immobilization of IBA. Despite the well-studied demonstration, there are still challenges of second-water pollution, high treatment cost, and unstable durability. Hydrothermal treatment has been reported to effectively stabilize IBA in several studies [28,29]; however, its high energy consumption and process complexity significantly hinder large-scale industrial application.

A promising strategy to mitigate the leaching risks of IBA involves its weathering through natural carbonation, which has been demonstrated to effectively reduce heavy metal release to meet regulatory limitations [30,31]. This approach is attractive due to its low cost and its potential contribution to carbon capture and storage [32]. The underlying carbonation chemistry facilitates the immobilization of trace metals by lowering the system pH, inducing the precipitation of metal carbonates (e.g., $PbCO_3$, $CdCO_3$, $ZnCO_3$), and promoting adsorption onto newly formed $CaCO_3$ phases, thus reducing their release [33]. While natural carbonation has been widely recognized for its environmental benefits, its excessively long treatment timeframe significantly limits practical and large-scale application (Fig. 1). To overcome this limitation, accelerated carbonation treatment has been intensively investigated as an effective route to immobilize IBA leaching behaviour [34–37]. For instance, Rendek et al. [38] reported that accelerated carbonation decreased the pH value of IBA from approximately 11.8 to 8.2, thereby efficiently suppressing the leaching of major heavy metals, including Pb, Cr, and Cd. However, a critical challenge remains: soluble salts, particularly chloride and sulfate, are not effectively immobilized and can even be readily released [39], posing persistent environmental risks. Thus, developing an advanced accelerated carbonation strategy that can simultaneously immobilize heavy metals and soluble salts, while remaining cost-effective and scalable for industrial implementation, is essential for the sustainable utilization of IBA.

Recently, the carbonation coating (CC) technique has emerged as a forward-looking strategy for tailoring the surface morphology and functional properties of particulate materials. In contrast to conventional accelerated carbonation, which primarily involves bulk mineral carbonation of the entire material through gas-solid or gas-liquid-solid reactions, the CC approach focuses on surface modification via heterogeneous nucleation and crystallization. Specifically, this approach enables the in-situ growth of $CaCO_3$ shells on host particle surfaces through mass transfer at the solid-liquid interface, resulting in a core–shell architecture. This structure-fabricated process not only alters surface roughness but also provides physical encapsulation, enhancing material functionality. For instance, $CaCO_3$ generated in a $Ca(OH)_2$-H_2O-CO_2 carbonation system has been deposited onto wollastonite surfaces, producing a roughened morphology with blunted edges that significantly improves filler dispersion, mechanical performance, and consistency in plastic composites [40]. Similarly, Fan et al. [41,42] employed the CC technique to fabricate $CaCO_3$@fly ash core-shell structures while simultaneously producing precipitated calcium carbonate (PCC). This process achieved substantial brightness enhancement, enabling their application as paper fillers. Inspired by these advances, the CC-induced core–shell architecture presents a promising strategy for IBA stabilization, as it integrates physical encapsulation with carbonate precipitation to suppress contaminant migration and release. As illustrated in Fig. 1, compared with traditional carbonation approaches, which typically involve long reaction times and the leaching of certain pollutants, the aqueous CC process proceeds over a much shorter timeframe and enables the encapsulation of a broad range of contaminants, while simultaneously generating high value-added PCC. Furthermore, through the concurrent utilization of municipal solid waste incineration bottom ash and incineration flue gas, CC technology offers both environmental and economic benefits. However, to the best of our knowledge, the application of the CC concept to IBA remains limited, and the underlying CC reaction kinetics remain insufficiently studied and warrant further investigation. Furthermore, despite the cost-effectiveness and environment benefits associated with employing waste IBA to replace building aggregate, the futural industrial operation of CC process, especially the usage of both dedicated equipment and commercial chemical agents, may increase energy operation and operation cost, consequently

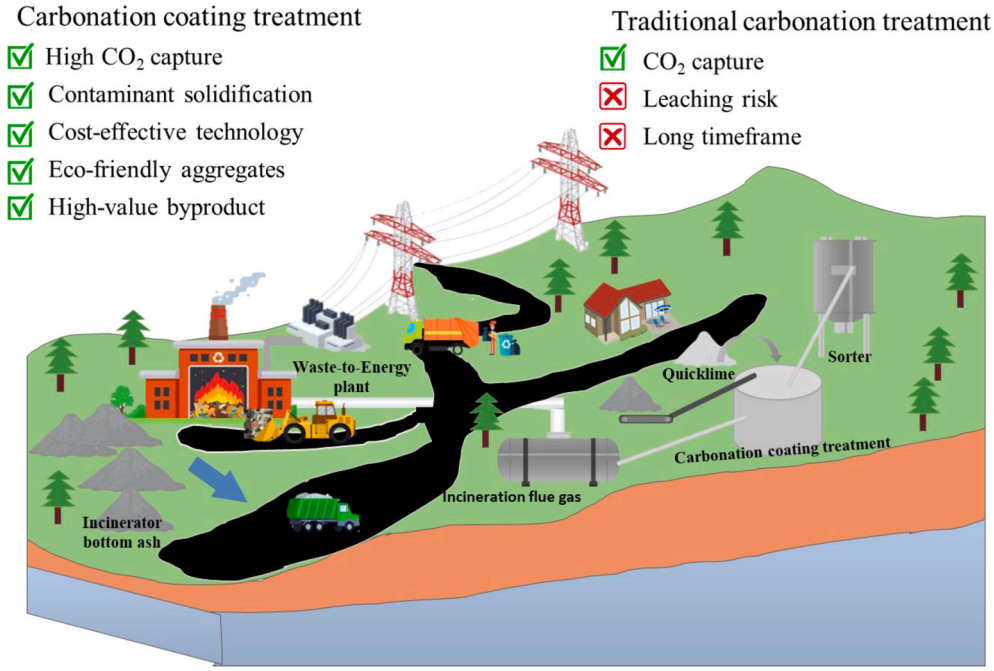

Fig. 1. Schematic illustration of industrial carbonation coating treatment route.

potentially offsetting sustainable benefits. To date, systematic investigation remains scarce regarding whether the IBA aggregates undergoing CC treatment can truly achieve economic efficiency, carbon reduction, and environmental sustainability across their full life cycle.

Herein, we report an environmentally friendly and efficient strategy, carbonation coating treatment, to immobilize contaminants in IBA through the construction of a core-shell architecture. Unlike conventional carbonation treatments of IBA reported in the literature [34, 43–45], which primarily focus on reducing alkalinity and immobilizing partial heavy metals, certain toxic elements and soluble salts (e.g., chlorides and sulfates) are often insufficiently stabilized and may even exhibit increased leaching due to pH reduction. Consequently, multiple treatment steps are typically required, leading to increased processing complexity and cost. Moreover, existing carbonation approaches rarely achieve simultaneous immobilization of the full spectrum of contaminant ions. Accordingly, the motivations and novelty of this study are to: (1) investigate the feasibility of simultaneously immobilizing diverse contaminant ions via a $CaCO_3$ core-shell structure formed using CC technology; (2) study the mechanical performance and leaching behavior of resulting mortar composites; and (3) assess the economic and environmental feasibility of scaling up the CC process for practical applications. The resulting core-shell aggregates ($CaCO_3$@IBA) were systematically evaluated for their feasibility as fine aggregate substitutes for natural sand. In this study, X-ray photoelectron spectroscopy (XPS), transmission electron microscope (TEM), and scanning electron microscopy (SEM) confirmed the successful formation of the core-shell structure. A modified surface coverage model was employed to reveal the microreaction kinetics of the CC process. Leaching test, combined with molecular dynamics (MD) simulations, revealed the contaminant immobilization mechanisms introduced by the CC treatment on IBA aggregates. In addition, the mechanical strength, microstructure, and leaching behavior of the resulting mortar composites were comprehensively investigated. Furthermore, economic and environmental assessments were conducted to evaluate the feasibility and sustainability of the proposed CC process for future industrial implementation. Overall, this study demonstrates a sustainable pathway for producing stabilized IBA aggregates coupled with value-added $CaCO_3$ fillers, addressing critical challenges associated with the sustainable utilization of incineration residues in the construction sector.

2. Materials and methods

2.1. Materials

The IBA aggregates were collected from a local incineration plant (Heros Sluiskil, the Netherlands). IBA particles with sizes smaller than 2 mm were selected for this study based on two considerations. First, this particle size range provides a distribution comparable to that of natural fine aggregate sands. Second, potentially hazardous elements are preferentially enriched in the finer IBA fractions [22], whereas coarser particles generally exhibit lower contaminant levels. Targeting fine IBA therefore addresses potential environmental risks, thereby enabling resource utilization of the most contaminated fraction. Accordingly, the IBA was sieved to obtain particles smaller than 2 mm. The sieved IBA exhibited a pH of 13.07. Its fineness modulus was 3.7, comparable to that of standard sand (3.2), indicating considerable potential as a sand substitute.

The chemical composition of IBA, summarized in Table 1, is dominated by SiO_2, CaO, and Al_2O_3. Such a composition is consistent with values reported in previous studies [10,46]. Trace heavy metals were also detected, including 7.12 mg/kg ds of Cu, 1.74 mg/kg ds of Ba, and 1.08 mg/kg ds of Cr, along with high concentrations of harmful salts such as 9220 mg/kg ds of chloride and 1150 mg/kg ds of sulfate. These contaminants necessitate effective treatment measures to prevent potential environmental pollution. In addition, analytical reagent grade calcium hydroxide ($Ca(OH)_2$) was used as the reactant in this study, exhibiting a purity of 93.6 wt%, a median particle size (D_{50}) of 5.4 μm, and a BET specific area of 14.8 m^2/g.

Table 1
Chemical compositions of raw materials and contaminant ions leaching of IBA.

Chemical composition	CEM I 52.5 R (wt%)	IBA (wt %)	Standard sand (wt%)	Hazardous element	Leaching value of IBA (mg/kg_{ds})
SiO_2	15.8	37.9	92.0	Cu	7.12
CaO	68.2	22.0	0.2	Zn	0.61
Al_2O_3	6.9	13.8	5.9	Ba	1.74
Fe_2O_3	3.9	17.7	0.1	Cr	1.08
MgO	1.2	1.5	-	Mo	0.79
K_2O	1.5	1.3	0.5	Chloride	9220
SO_3	2.8	1.2	0.1	Sulfate	1150
CuO	-	0.7	-		
ZnO	-	1.0	-		
LOI	1.4	8.1			

2.2. Test methods

2.2.1. Preparation method of $CaCO_3$@IBA

Prior to treatments, IBA was oven-dried at 105 °C for 24 h. The carbonization coating (CC) route is illustrated in Fig. 2. The dried IBA was thoroughly mixed with $Ca(OH)_2$ powder at a solid-solid mass ratio of 1:1, after which distilled water was added to achieve a liquid-solid mass ratio of 10:1 under continuous stirring. These mixture ratios followed the optimal conditions reported by Fan et al. [47]. To enhance the CC effect, the stirring speed was set at 400 rpm. A higher speed would risk detaching the freshly formed coating layer, whereas a lower speed would hinder adequate slurry dispersion. The pH of the suspension was monitored in real time using a calibrated pH meter. CO_2 gas was introduced at the bottom of the reaction vessel at a constant flow rate of 2 L/min. Injection of CO_2 initiated an immediate reaction with $Ca(OH)_2$, as indicated by a rapid decrease in pH (see Fig. S1). The formation of $CaCO_3$ guest particles was judged to be completed when the pH value reached 7. The obtained slurry was filtered using a suction filtration device, and the retained solids were dried overnight at 105 °C. Finally, the main product, $CaCO_3$@IBA aggregates, and by-product precipitated calcium carbonate (PCC, $CaCO_3$) were separated by sieving. The $CaCO_3$@IBA aggregates approximately accounted for 76.3 wt%. The corresponding CC reaction mechanism was discussed later.

2.2.2. Mortar composite preparation

The IBA and $CaCO_3$@IBA aggregates were used as partial replacements for natural sand in mortar composites at volume replacement levels of 10% and 30%. The detailed mix proportions are presented in Table 2. Mortar prepared exclusively with standard sands served as the reference mixture. All mortars were produced using a Hobart planetary mixer with a cement/fine aggregates mass ratio of 1:2. The respective mortars were labelled as “IBAM” (IBA-blended mortar), “CIBAM” ($CaCO_3$@IBA-blended mortar), and “PSM” (pure sand mortar). Considering the water absorption capacity of the fine aggregates, additional water was added to compensate for the absorbed amount in order to maintain a constant effective water-to-cement (w/c) ratio of 0.5. This approach was adopted to eliminate the influence of variations in the w/c ratio caused by aggregate water absorption on the experimental results.

Fresh mortars were cast into 4 cm × 4 cm × 16 cm prism moulds and vibrated to emit the entrapped air. After 24 h of initial curing, the specimens were demoulded and transferred to be cured in a controlled environment room maintained at 23 °C and 65% relatively humidity. Mechanical strength tests were conducted after curing periods of 3 and 28 days.

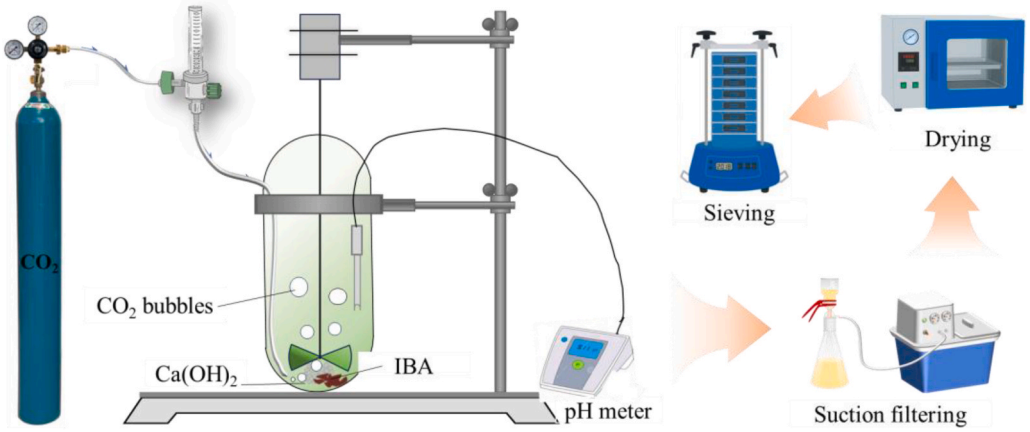

Fig. 2. Schematic diagram of the carbonation-coating route of IBA.

Table 2
Mix proportions.

ID number	Mix proportion (kg/m^3)				
	Cement	Standard sands	IBA	$CaCO_3$@IBA	Effective water[a]
PSM	636	1272	-	-	318
IBAM10	625	1166	85	-	313
IBAM30	603	941	265	-	301
CIBAM10	635	1148	0	122	317
CIBAM30	632	897	-	367	316

[a] Total - (water absorbed in aggregates).

2.3. Characterization techniques

2.3.1. Basic property characterization

IBA was oven-dried at 105 °C until a constant mass was achieved prior to testing. Water absorption content was determined following the procedure described by Tang et al. [48]. Particle size distributions of the IBA and $CaCO_3$@IBA aggregates were measured by sieve analysis in accordance with ASTM-C136. The true densities of both aggregates were measured using a Micrometric AccuPyc II 1340 helium pycnometer. Pore size distribution was characterized by nitrogen adsorption-desorption isotherms using a Brunauer-Emmett-Teller (BET) specific surface area and porosity instrument (TriStar II 3020, Micrometric). Nitrogen (N_2) was used as the adsorbed gas at −196 °C, and samples were degassed at 200 °C prior to analysis. The specific surface was calculated from the adsorption branch of the isotherm using the BET method described by Joyner et al. [49]. At least three parallel specimens were prepared and tested for each set of experimental results.

2.3.2. Microstructure characterization

The microstructure and surface elemental composition of IBA and $CaCO_3$@IBA were examined using scanning electron microscopy coupled with energy-dispersive spectroscopy (SEM-EDS, JOEL JSM-5600) at an accelerating voltage of 15 kV. The crystallographic phase composition of both samples was qualitatively analyzed using an X-ray diffractometer (XRD, Bruker D8 Venture) with Cu Kα radiation over a 2θ range of 5° to 90° at a scanning speed of 1°/min. Fourier-transform infrared (FTIR) spectroscopy was performed using a Varian 3100 Spectrometer with 30 scans at a resolution of 1 cm^{-1}. The surface chemical bonding states and binding energies of C 1s, O 1s, and Ca 2p elements of the $CaCO_3$@IBA sample were analyzed using an XPS (Thermo Scientific Kα, USA). The core-shell structure of $CaCO_3$@IBA was further characterized by TEM (Talos F200X), and the elemental composition was identified using energy-dispersive spectroscopy (EDS, SuperXG2) at an acceleration voltage of 200 kV. Thermogravimetric analysis (TGA) was employed to quantitatively calculate the CO_2 sequestration amount of both IBA and $CaCO_3$@IBA samples. Prior to testing, the samples were ground into fine powders, and approximately 15 mg of each sample was heated from 30 °C to 1000 °C at a constant heating rate of 10 °C/min under a nitrogen flow of 30 mL/min. To truly quantify the CO_2 uptake efficiency, the carbonation-coating efficiency $\delta_{CC}(\%)$, of the $CaCO_3$@IBA aggregates was calculated based on the 100 g IBA sample using the following equation:

$$\delta_{CC}(\%) = \frac{m_{co_2\ upt\ of\ CaCO_3@IBA}}{\Delta m_{CO_2}} \quad (1)$$

Where $m_{co_2\ upt\ of\ CaCO_3@IBA}$ denotes the mass of CO_2 uptaken by the $CaCO_3$@IBA aggregates, which can be calculated based on TGA results; Δm_{CO_2} represents the mass decrease of the CO_2 gas cylinder during CC reaction.

2.3.3. Mechanical properties test

Compressive and flexural strength tests were carried out according to EN196-1 [50]. The reported results represent the mean values obtained from three replicate specimens.

2.3.4. Leaching behavior test

A standard leaching test was conducted on the aggregate (IBA and $CaCO_3$@IBA) and the resulting crushed mortar samples, following the procedure of EN 12457-2 [51]. The hardened mortars were crushed and sieved to obtain particles smaller than 4 mm. Each sample was then mixed with distilled deionized water at a liquid-to-solid ratio of 10:1 and agitated for 24 h at 300 rpm. Following agitation, the suspension was filtered through a 0.45 μm membrane filter, and the filtrate was divided into two equal portions. One portion was acidified with about one or two drops of 98% HNO_3 for cation analysis by inductively coupled plasma mass spectrometry (ICP-MS). The other portion was used directly for anion analysis (chloride and sulfate) by ion chromatography (IC).

2.3.5. Molecular dynamics simulation

Classic molecular dynamics (MD) simulations were carried out to investigate, at the atomic level [52], the absorption and binding behavior of vaterite-type $CaCO_3$ (see Fig. S2) toward contaminant ions released from IBA during the CC process. Vaterite $CaCO_3$ was selected because it is the initial metastable polymorph formed. Initial configurations of solvent systems were generated using the PACKMOL software. A specially developed force field based on the generalized OPLS-AA framework was employed. In this simulation, nonbonded interactions in the molecular force field, including van der Waals and electrostatic interactions, were considered. Atomic motions were governed by classical Newtonian mechanics and integrated using the velocity-Verlet algorithm. All MD simulations were performed using the GROMACS

simulation package.

2.4. Sustainability models

2.4.1. Industrial-scale process design

Building on the laboratory-scale experiments, an integrated process was designed to assess the feasibility of applying CC treatment of the IBA at an industrial scale (Fig. 12). Overall mass balance is provided in Table S1. The proposed plant is designed to process 100 tons per day of as-received IBA from a Waste-to-Energy (WtE) plant, together with 250.1 m^3 per day of incineration waste gas from the same source. The ratio of incineration waste gas to IBA was determined by considering the CO_2 uptake capacity of IBA during the laboratory-scale CC reactions. The CO_2 content of the incineration waste gas was assumed to be 12 vol % (equivalent to 18.4 wt%) based on the literature data [38]. For the industrial-scale process, the effective CO_2 uptake efficiency was assumed to be 95 wt% of the value achieved under laboratory conditions.

2.4.2. Cost-benefit analysis

To evaluate the commercialization potential of the scale-up process, a cost-benefit analysis was performed using a probabilistic approach to account for the inherent variability and uncertainty of economic parameters. Triangular distributions were applied to key economic factors and evaluated using Monte Carlo simulation with 10^6 iterations. The analysis included:

- Capital costs, such as land lease cost and equipment purchase (see Table S2).
- Operating expenditures, including raw material cost (e.g., water cost and quicklime cost), transportation, labour cost, depreciation & maintenance, and wastewater treatment.
- Revenue streams, including avoided cost (e.g., saved gate fees & landfill tax and saved CO_2 tax), income from the main product ($CaCO_3$@IBA aggregate), and income from by-product PCC;
- Key financial parameters, such as the discount rate.

The CO_2 tax was projected to increase by 15% annually based on Dutch carbon tax policy [53], while the depreciation and maintenance cost was assumed to rise by 12% per year, considering progressive equipment degradation. The lower limit, mode, and upper limit were used for the triangular distribution of each economic parameter (Table S3).

Two key financial indicators-net present value (NPV) and benefit-cost ratio (BCR) were used to evaluate the cost-benefit performance of the industrial-scale CC process [34,54]. Their calculations are expressed as follows:

$$NPV = \sum_{t}^{Lt} \frac{C_t}{(1+r)^t} - C_0 \tag{2}$$

$$BCR = \frac{NPV}{\sum_{t}^{Lt} \frac{C_{ot}}{(1+r)^t}} + C_0 \tag{3}$$

Where Lt is the operation period (10 years), C_t is the net cash flow in year t, C_0 is the initial capital cost; r is the discount rate modelled as a triangular distribution in the Monte Carlo simulation with a lower limit (5%), mode (6%), and upper limit (8%), C_{ot} represents the cash outflows in year t. The Monte Carlo simulation was carried out in Microsoft Excel using the @RISK software package [55].

2.4.3. Environmental impact analysis

To evaluate the environmental impact of the scale-up process, a life cycle assessment (LCA) analysis was conducted using the SimaPro 9.4.0.1 software package [56].

Goal and scope definition: The goal is to investigate the environmental impact of producing $CaCO_3$@IBA aggregates at an industrial scale. To avoid the complications related to the product market distribution and end-use scenarios, the cradle-to-gate LCA approach was adopted [57], as shown in Fig. 3. This approach covers the environmental impacts from raw material acquisition through to the product producing stage. In addition, the following assumptions were considered:

1. A baseline target process of 1 ton of final $CaCO_3$@IBA product.
2. As this study mentions transportation distance between the carbonation treatment factory and the WtE plant was fixed at 5 km, considering the convenience of utilizing the IBA and incineration flue gas, as well as the relevant cost savings.

System boundaries: The stages include the transportation of the IBA to the carbonation treatment factory, the unit processes involved in raw materials preparation, the treatment stages, and the energy generation required to support each operation.

Functional unit: The functional unit was taken as 100 tons of wet IBA through an industrial-scale CC treatment process for the $CaCO_3$@IBA aggregate production.

Impact assessment: The potential environmental impacts were evaluated based on the inventory analysis data (see Table S4), which is associated with impact categories and indicators [58–60]. To simply understand the environmental impact of each stage, some of the units are classified. In detail, pre-treatment mainly represents units before CC treatment, including RD-1, SM-1, CC, BC-1, CP-1, and CP-2; post-treatment primarily means units after CC treatment, including CP-3, FP, RD-2, SM-2, and BC-2. The impact assessment was carried out using the ReCipe midpoint (H) method. The assessment of GWP for the global scale-up of the CC pilot was conducted based on the available data on municipal solid waste generation across 17 countries/regions in 2022 (see Table S5) and the amount of Dutch IBA in 2022 (see Table S6).

3. Results and discussion

3.1. Performance of $CaCO_3$@IBA aggregates

3.1.1. Physicochemical properties

The schematic illustration (Fig. 4a) demonstrates the preparation process of $CaCO_3$@IBA, which follows the heterogeneous nucleation and crystallization process described by the LaMer model theory [61]. Initially, the monomer concentration of $CaCO_3$ increases and then transforms into clusters as the carbonation reaction proceeds. Once the concentration exceeds the critical supersaturation level, $CaCO_3$ preferentially undergoes heterogeneous nucleation on the surface of the IBA, as heterogeneous nucleation requires a lower energy barrier than homogeneous self-nucleation. Nonetheless, part of the generated $CaCO_3$ monomers do not have sufficient time to deposit onto the IBA surface and instead undergo homogeneous nucleation and self-crystallization, forming by-product free precipitated calcium carbonate (PCC, $CaCO_3$) particles. Considering that the aqueous carbonation route for PCC production is a mature technology, the present study focuses on the main product, $CaCO_3$@IBA, as the primary research objective. Through the CC treatment, the IBA was encapsulated by a $CaCO_3$ shell layer. Although a slight rightward shift in the particle size distribution is observed (Fig. 4b), the overall grading curve shape remains comparable to that of natural sand, and the particle size range continues to fall within the fine aggregate classification. Thus, CaCO3@IBA retains its potential as a substitute for fine aggregate sand. Regarding densities (Table 3), the micro-/nano calcium carbonate nucleation and crystallization growth on the IBA surface lead to a slight increase in particle density, reaching approx. 1.45 g/cm^3 in bulk density and approx. 2.53 g/cm^3 in true density, respectively. Similarly, the D50 and D90 particle diameters increased to 1.04 mm and 2.76 mm, respectively. On the other hand, significant reductions in the SSA (39.25%) and water absorption

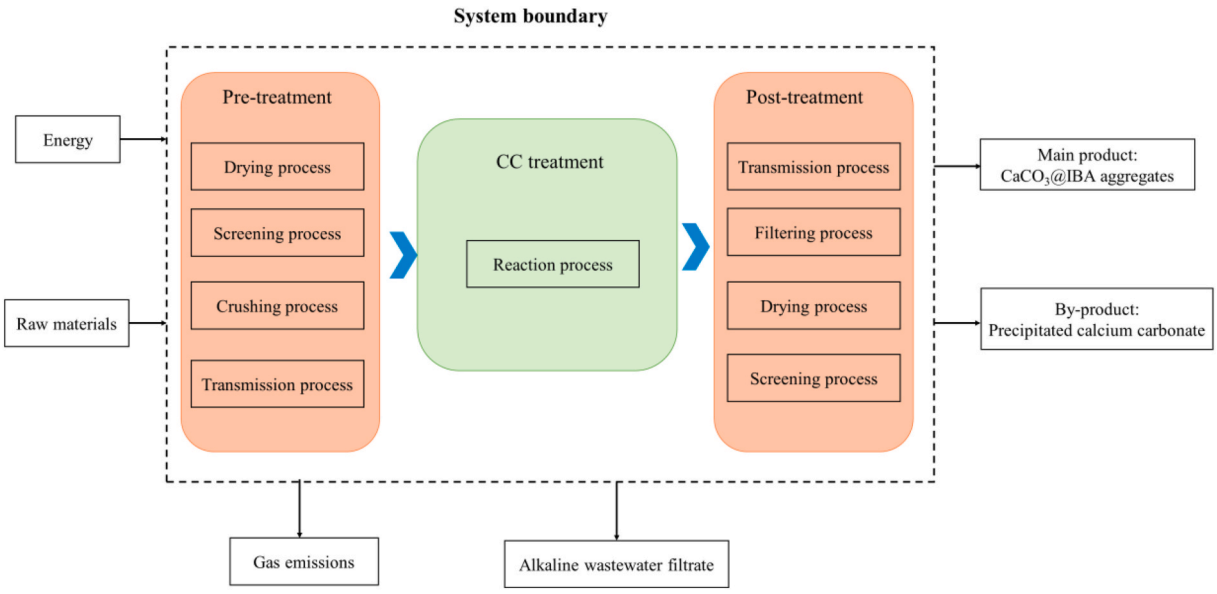

Fig. 3. LCA system boundary.

rate (57.1%) have been observed due to the growth of IBA aggregates.

To reveal the evolution in surface chemical properties, FTIR and XPS were used to characterize the surface chemical morphology of IBA before and after CC treatment. Several distinct differences of FTIR spectra are observed in Fig. 4c, implying critical chemical structural transformations. The peak appearing at around 3459 cm^{-1} corresponded to the absorbed water molecules [62]. The band at approximately 1650 cm^{-1} is related to the deformation mode of the surface hydroxyl group [63,64]. These peaks become weaker or even disappear in $CaCO_3$@IBA, reflecting the reduced hydrophilic performance. This is consistent with the water absorption capacity measurement (Table 3). The bands at 1424 cm^{-1}, 875 cm^{-1}, and 710 cm^{-1} are related to vibrations of carbonates (CO_3^{2-}) [65,66]. These bands are most intense for $CaCO_3$@IBA, which corresponds to newly formed $CaCO_3$. The IBA after CC treatment exhibits a weak peak signal at around 1100 cm^{-1}, corresponding to asymmetric stretching vibrations of Si-O-Si(Al) [67]. The presence of this weak peak in $CaCO_3$@IBA is likely attributable to disruption caused by compression during sample preparation. Subsequently, XPS was employed to reveal the chemical states of elements in aggregates, IBA, and $CaCO_3$@IBA aggregates. The full XPS survey spectra in Fig. 4d verify the presence of only C, O, and Ca elements in the $CaCO_3$@IBA compared to complex elements Si, C, O, Ca, Al, and Na present on the IBA surface. The C1s spectrum of $CaCO_3$@IBA exhibits three prominent peaks at 284.8, 286.8, and 289.1eV, corresponding to the C-C (65.35%), C-O (5.24%), and CO_3(29.41%), respectively. The two peaks located at 534.3 and 532.1 eV correspond to C-O (5.99%) and C=O (94.01%), respectively. The Ca2p spectrum presents two prominent peaks at 350.9 and 347.3 eV, corresponding to the Ca $2p_{1/2}$ (32.76%) and Ca 2p3/2 (67.24%)of $CaCO_3$@IBA. These findings collectively confirm the successful formation of shell-layer $CaCO_3$ on the IBA surfaces by the CC treatment.

TEM images in Fig. 4e reveal a distinct core-shell architecture. The shell thickness more than 300 nm was observed in the HRTEM image (Fig. 4g). Combined with the morphological evolution via SEM image observation (Fig. 4k), cauliflower-like shell growth on the IBA surfaces was observed. Such a core-shell structure not only enhances contaminant immobilization through encapsulation structure but also ensures maximal strength of resulting mortar composites by strengthening mechanical interlocking at the aggregate-matrix interface. Energy dispersive X-ray spectroscopy (EDS) mapping (Fig. 4f)and element atomic percentage evolution (Fig. 4k) after the CC treatment confirmed the uniform distribution of C, O, and Ca elements throughout the IBA surface (Fig. 4f), further illustrating the homogeneous deposition of $CaCO_3$ micro-/nanoparticles on the IBA surface. To clarify the crystal structure of the $CaCO_3$ shell, HRTEM analysis (Fig. 4h) reveals three distinct sets of lattice fringes with interplanar spacings of 0.23, 0.30, and 0.25 nm, corresponding to the (113), (104), and (110) crystallographic planes of cubic $CaCO_3$, respectively. Simultaneously, Selected area electron diffraction (SAED) patterns (Fig. 4j) clearly identified the (104), (110), and (116) crystallographic planes of rhombohedral $CaCO_3$. X-ray diffraction (XRD) results (Fig. 4l) showed diffraction peaks at 23.0°, 29.4°, 36.0°, 39.4°, 43.1°, 47.5°, and 48.5° of pure rhombohedral $CaCO_3$, respectively. This further corroborates this conclusion from another perspective.

The CO_2 sequestration of the $CaCO_3$@IBA and IBA aggregates was evaluated by TG analysis (Fig. 4m). Specifically, four mass-loss stages for both aggregates were classified: 40-130 °C, 130-370 °C, 370-620 °C, and 620-760 °C. The first mass-loss stage corresponds to the unbonded water evaporation [68]. In the initial stage, compared to the $CaCO_3$@IBA, the mass loss of the IBA is relatively higher, around 2%, with a more pronounced DTG peak in this region. This is probably attributed to higher water absorption capacity. In the II stage, the IBA continued to show a slightly greater mass loss, which can be ascribed to the release of chemically bound water from calcium sulfate dihydrate (gypsum) [68–70]. No peak observed in the III degradation regime, which indicates that little portlandite and vaterite exist in the IBA and $CaCO_3$@IBA aggregates, respectively. Finally, the sharp peaks from 620 to 800 °C, corresponding to the calcium carbonate decomposition [38], were observed in the IV stage. This stage provides insight into the amount of trapped carbon dioxide for CO_2 sequestration content that were calculated as 246.45 mg CO_2/g IBA, which can used for δ_{CC} calculation. Furthermore, the TGA and DTG results indicate that the $CaCO_3$ content in $CaCO_3$@IBA is significantly higher than that in IBA after the CC treatment. This suggests that additional $CaCO_3$ mineral phases were formed via exogenous calcium ($Ca(OH)_2$)-driven heterogeneous crystallization on the IBA surface. These findings are in good agreement with the XRD results, which show enhanced calcite-related diffraction peaks after the CC treatment.

The above physicochemical characterizations confirm the successful formation of the $CaCO_3$@IBA core–shell structure through the CC technique. However, these results mainly reflect the final state of the CC process and do not provide insight into the dynamic evolution of $CaCO_3$ deposition on the IBA surface. Thus, the CC reaction kinetic analysis is required to further elucidate the dynamic formation mechanism of the

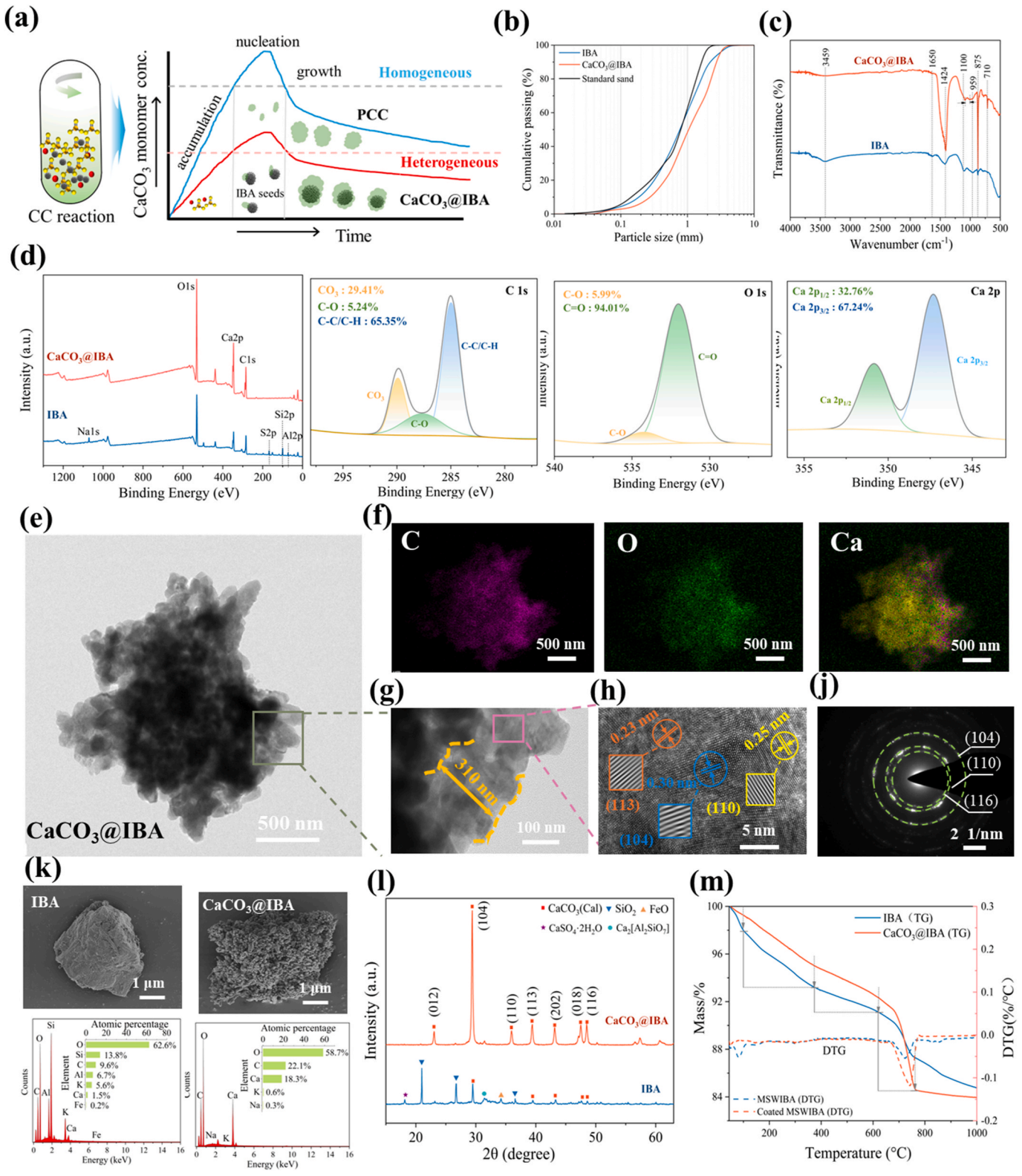

Fig. 4. Physicochemical performance panel. (a) Schematic illustration of the CC procedures for $CaCO_3$@IBA; (b) PSD curves of the samples: stand sands, IBA, and $CaCO_3$@IBA; (c) FTIR patterns between IBA and $CaCO_3$@IBA; (d) The XPS broad spectrum of IBA and $CaCO_3$@IBA, corresponding with high-resolution XPS spectra of C1s and O1s and Ca2p of $CaCO_3$@IBA; (e)TEM image, (f) elemental mapping images, (g) & (h) HRTEM images (the inset showing the lattice spacing), (j) SAED pattern of $CaCO_3$@IBA; (k) SEM with EDS images, (l) XRD pattern and (m) TG with DTG curves of IBA and of $CaCO_3$@IBA.

Table 3
Basic properties of IBA, $CaCO_3$@IBA, and standard sand.

Samples	Bulk density (g/cm^3)	True density (g/cm^3)	SSA (BET, m^2/g)	Water absorption (%)	d (0.5) (mm)	d (0.9) (mm)
IBA	1.02 ± 0.02	1.74 ± 0.01	5.86 ± 0.04	35.2 ± 0.5	0.76	2.33
$CaCO_3$@IBA	1.45 ± 0.03	2.53 ± 0.03	3.56 ± 0.02	15.1 ± 0.2	1.04	2.76
Standard sand	1.61 ± 0.02	2.65 ± 0.03	0.67 ± 0.01	0.2 ± 0.1	0.79	1.61

core–shell structure.

3.1.2. *Carbonation coating reaction kinetics*

Subsequently, the CC reaction kinetics of the IBA in the gas-liquid-solid three-phase system were systematically investigated. The overall CC kinetic process comprises sequential mass-transfer and reaction stage, including CO_2 gas dissolution and dispersion in the liquid phase, gas-liquid transfer, optional $Ca(OH)_2$ dissociation and dispersion in the liquid phase, and carbonation-coating reaction in which $CaCO_3$ forms and precipitates on the IBA surface (Fig. 5a). The corresponding microscopic molecular pathway across the three phases is illustrated in Fig. 5b, which can be divided into three steps. (1) CO_2 diffusion and dissolution: CO_2 dissolves in water and is hydrated to form H_2CO_3 (Eq. (4)), which subsequently ionizes to yield CO_3^{2-} (Eqs. (5) and (6)). (2) Carbonation-coating reaction: the generated CO_3^{2-} ions reacted primarily with Ca^{2+} in the water film, leading to heterogeneous nucleation and crystallization of $CaCO_3$, which then precipitates onto the IBA particle surfaces (Eqs. (7)–(9)).

$$CO_2\ (g) + H_2O \rightarrow H_2CO_3 \quad (4)$$

$$H_2CO_3\ (aq) \rightarrow HCO_3^- + H^+ \quad (5)$$

$$HCO_3^- \rightarrow CO_3^{2-} + H^+ \quad (6)$$

$$Ca(OH)_2\ (s, addition) \rightarrow Ca^{2+} + 2OH^- \quad (7)$$

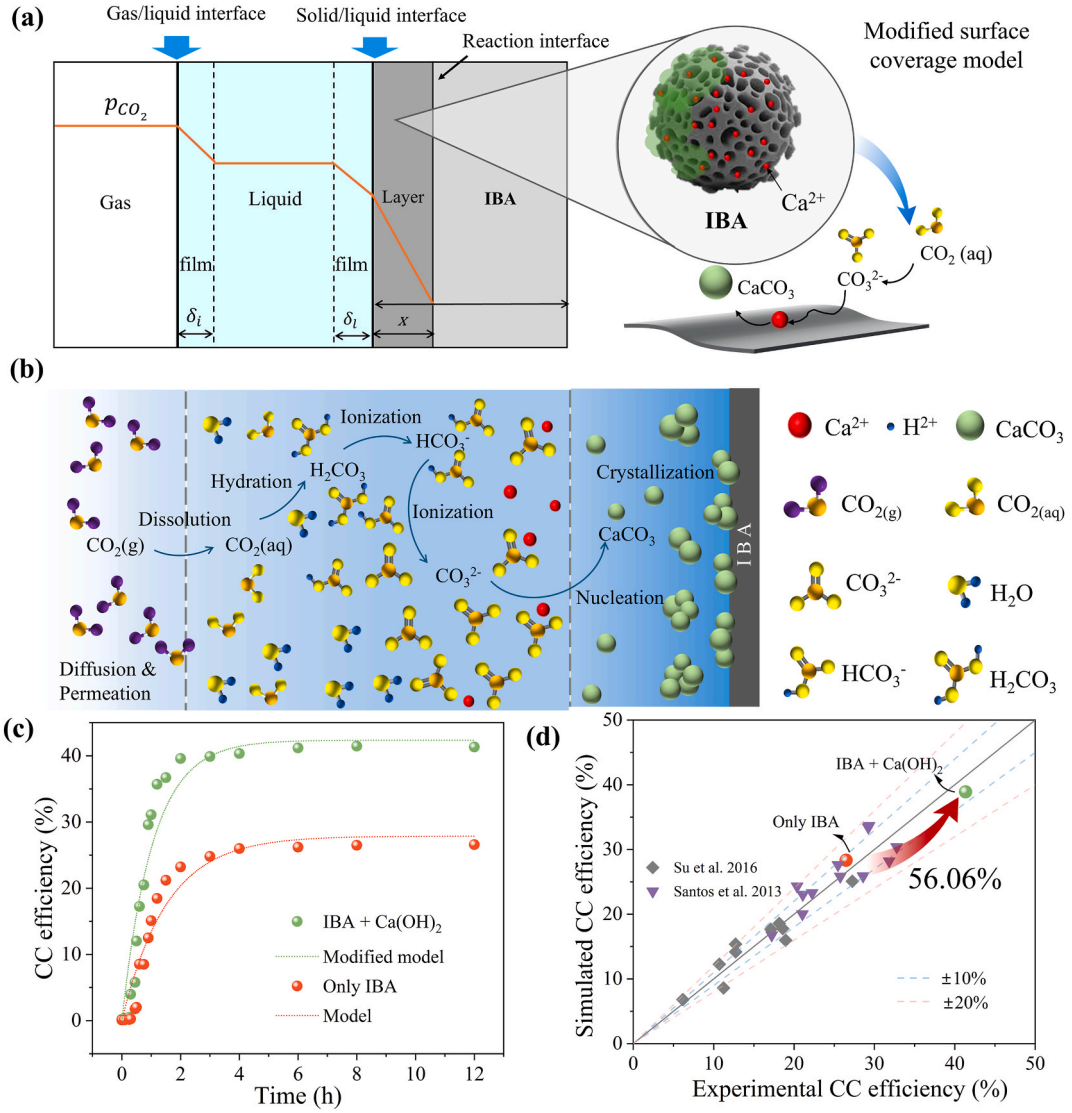

Fig. 5. (a) Schematic illustration of the CC reaction kinetic process. (b) Microscopic molecular-scale dynamic reaction process. (c) CC efficiency curves and corresponding kinetic model fits for IBA alone and for IBA supplemented with $Ca(OH)_2$. (d) Comparison of the experimental and simulated results obtained in this study with reported data for other solid wastes [71,72].

$$Ca^{2+} + CO_3^{2-} \rightarrow CaCO_3 \text{ (nuclei)} \quad (8)$$

$$CaCO_3 \text{ (nuclei)} \rightarrow CaCO_3 \text{ (calcite)} \quad (9)$$

To determine the rate-controlling step in the CC reaction of IBA, ten commonly used solid-liquid models were fitted to the experimental data using the integral analysis method (Table S2). However, none of these models adequately described the reaction behaviour, as all yielded coefficients of determination (R^2) below 0.85. This indicated the need for a more appropriate model capable of capturing the characteristics of the carbonation-coating kinetics.

The carbonation-coating process described above, together with the observed formation of $CaCO_3$@IBA core–shell aggregates, is consistent with the assumptions of the surface-coverage model [73]: (1) the reaction product ($CaCO_3$) precipitates on the IBA surface; (2) the CC reaction occurs only at unreacted surface sites that remain uncovered by the precipitated product layer; and (3) the fraction of active surface sites (Φ) available for reaction decreases over time as a function of the reaction rate. On this basis, the surface-coverage model was adopted in this study.

Assuming that the rate-determining step of the CC process is the surface precipitation reaction, which occurs only at unreacted surface sites not covered by the $CaCO_3$ product layer, the reaction rate per unit initial surface area of the IBA can be expressed as:

$$r_s = k_s \Phi \quad (10)$$

Where k_s is the surface reaction rate constant ($mol \cdot h^{-1} \cdot m^{-2}$), which depends on temperature, the concentrations of the reacting species, and the relative humidity; and Φ is the fraction of surface sites (or surface area) that remain active and uncovered by the reaction product $CaCO_3$.

Accordingly, the rate of CC efficiency, $\delta_{cc}(\%)$, can be expressed as:

$$\frac{d\delta}{dt} = S_g M_{Ca} r_s = S_g M_{Ca} k_s \Phi \quad (11)$$

Where S_g ($m^2 \cdot g^{-1}$) is the specific surface area of IBA, and M_{Ca} (g/mol) is the weighted average mole mass of the calcium-bearing phases in both IBA and $Ca(OH)_2$. The term Φ is a function of time and characterizes the manner in which the $CaCO_3$ product is deposited on the IBA surface. Consequently, Φ varies over the course of the reaction and depends on the reaction rate. It can be expressed as:

$$\frac{-d\Phi}{dt} = k_p r_s = k_p k_s \Phi \quad (12)$$

Where k_p ($m^2 \cdot mol^{-1}$) is a proportionality constant, dependent on temperature, the concentrations of the reacting species, and the relative humidity. The constant reflects the fraction of surface area that remains reactive and is not yet covered by the product layer.

Integration of Eq. (12) gives Φ as a function of time. By defining $k_1 = k_s S_g M_{Ca}$ and $k_2 = k_p \cdot S_g^{-1} \cdot M_{Ca}^{-1}$, the expression becomes:

$$\Phi = \exp(-k_1 k_2 t) \quad (13)$$

Substituting Eq. (13) into Eq. (10) and integrating yields the relationship between the CC efficiency (δ_{cc}) and reaction times:

$$\delta_{cc} = \frac{[1 - exp(-k_1 k_2 t)]}{k_2} \quad (14)$$

The parameters values S_g, M, $k_s, k_p, k_1, and\ k_2$ used in the above equations are obtained in Table S7. Fig. 5c presents the model-fitting results for the CC process of IBA with and without $Ca(OH)_2$ addition. The experimental data are strongly correlated with the surface coverage model, with R^2 values exceeding 90%, confirming that the CC kinetics of IBA can be reliably described by this model. In both cases, the CC efficiency increases rapidly at the beginning of the reaction and then approaches a steady state. This behaviour indicates the rapid formation of a surface precipitate layer during the early stage of carbonation, which progressively hinders further reaction by blocking the remaining active sites on the IBA surface. This observation is consistent with previous literature reports [73]. As shown, a steeper slope and higher CC efficiency are obtained in the presence of $Ca(OH)_2$ compared with IBA alone. These results suggest that an increased supply of Ca^{2+} accelerates the carbonation reaction kinetics and provides additional active sites through the adsorption of Ca^{2+} onto the porous IBA surface. Specifically, the presence of $Ca(OH)_2$ enhances the CC efficiency of IBA by 56.06% (Fig. 5d). Moreover, compared with other solid wastes (e.g., stainless steel slags, basic-oxygen furnace slag) reported in the literature [71,72], the IBA investigated in this study exhibited a smaller standard error (±10%) between the simulated and experimental results. This might be related to the highly porous structure of IBA, which provides a greater number of accessible reaction sites and therefore conforms more closely to the assumptions of the surface-coverage model. These kinetic simulation results further support, from a theoretical perspective, the formation of the $CaCO_3$@IBA core-shell structure.

3.1.3. Immobilization behaviour and corresponding mechanism

The CC treatment of IBA aggregates is expected to influence their leaching behavior. Thus, leaching tests were performed on both IBA and $CaCO_3$@IBA aggregates. In Fig. 6a, all contaminant concentrations drop down, with significant reductions of 90% for Zn, 49% for Cu, 30% for chloride, 22% for Mo (in the form of MoO_4^{2-}). Other contaminant ions exhibited similar leaching trends, found in the supplementary information (Fig. S3a). It is worth noting that the reduction varies among different heavy metal elements, which is likely related to their element-specific chemical forms and binding characteristics [70,74]. Although the leaching results demonstrate that CC treatment can effectively immobilize contaminant ions, the underlying immobilization mechanism in the $CaCO_3$@IBA aggregates is still unclear. Theoretically, the immobilization mechanism can be explained by three pathways (Fig. 6b). First, the $CaCO_3$ crystal shells can act as a physical barrier by preventing the release of internal contaminants from the IBA aggregates and thereby reducing the leaching. Second, the CC treatment can decrease pH, promoting the formation of insoluble carbonates, thereby lowering their leaching. Finally, some heavy metal ions may be incorporated into $CaCO_3$ crystals through lattice substitution of Ca^{2+} and co-precipitation during shell-layer crystal growth [75,76]. The occurrence of doping and co-precipitation depends on the absorption capacity of $CaCO_3$.

To further investigate the adsorption performance, the adsorption behaviour of $CaCO_3$ toward different contaminant ions under aqueous carbonation conditions was studied. MD simulation is a useful tool for elucidating the adsorption behaviour of metal ions at mineral-water interfaces [77]; therefore, MD simulations were incorporated in this work. Simulation snapshots, taken at the final time of 10 ns, are shown in Fig. 6c. Zn ions were found to be located at the shortest distance from the $CaCO_3$ surface, whereas sulfates (SO_4^{2-}) were found to be the farthest distances (Fig. S3b). This observation is consistent with the number density profiles along the Z-axis (Fig. 6d and Fig. S3d). Fig. 6e and Fig. S3c represent the absorption energies, including van der Waals interaction energy and electrostatic energy. Metal cations (Zn, Ba, Cu) exhibit higher absorption energies than other contaminant anions such as chloride, MoO_4^{2-}, and CrO_4^{2-}. Combined with the mean square displacement (MSD) results (Fig. 6f and Fig. S3e), these findings indicate that heavy metal cations are readily and strongly adsorbed on the $CaCO_3$ phase surface, where they can substitute for Ca^{2+} and form insoluble carbonate phases co-precipitated with $CaCO_3$ crystals. This behaviour is attributed to the (101) and (104) crystallographic planes of the negatively charged $CaCO_3$ surface, which preferentially attract metal cations. In contrast, metal oxyanions such as MoO_4^{2-} and CrO_4^{2-} exhibit weaker adsorption, likely due to electrostatic repulsion and steric hindrance.

Overall, the MD simulations are in tune with the leaching experiment results. The CC treatment alters the leaching behaviour of IBA aggregates through their microstructure changes. These changes will likely influence the performance of cementitious mortars incorporating the

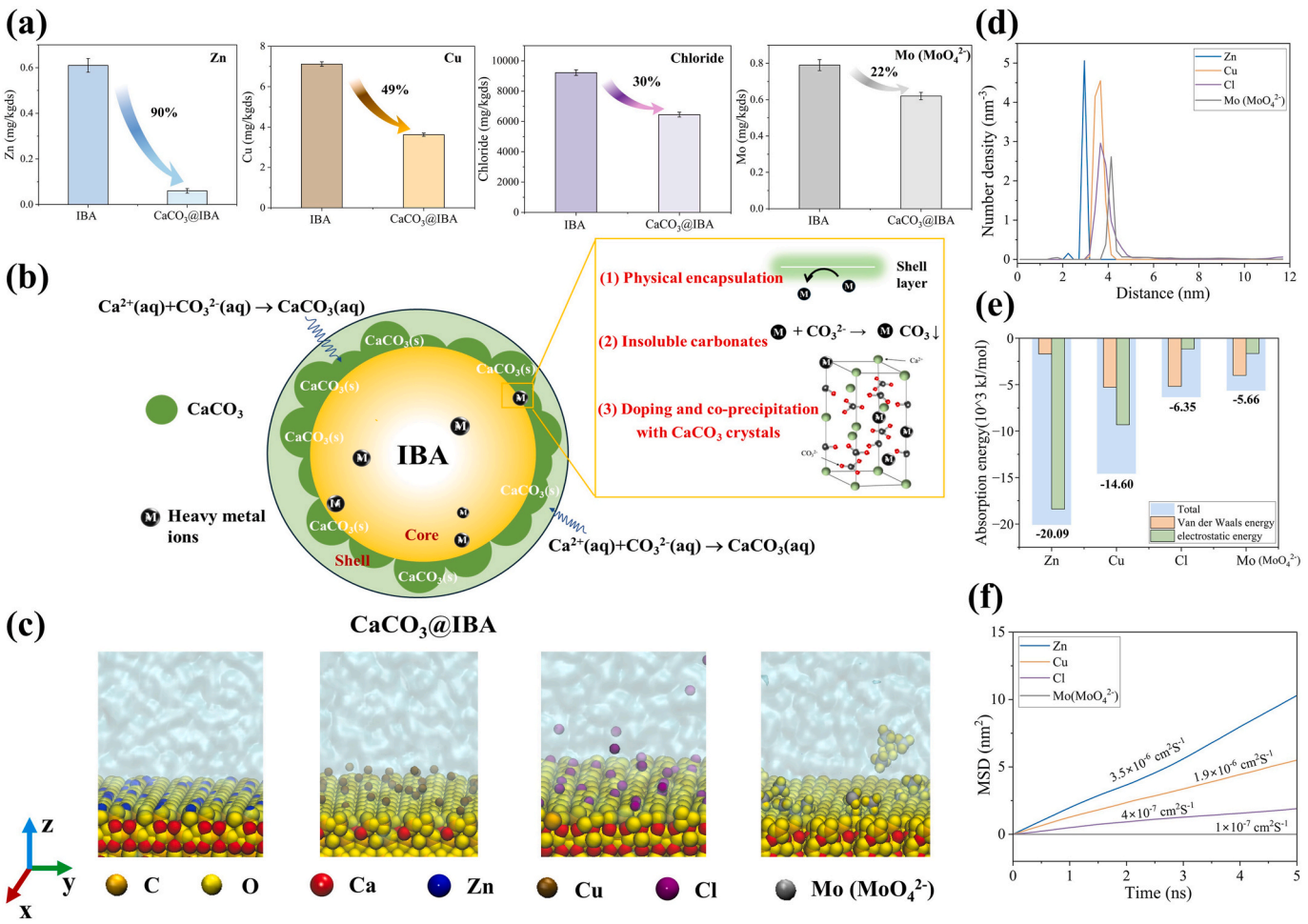

Fig. 6. Solidification effect panel. (a) Leaching behaviours of contaminant ions from the IBA and $CaCO_3$@IBA aggregates. (b) Schematic illustration of the immobilization mechanism of CC treatment on heavy metal ions in IBA. (c) Interfacial adsorption behaviour of $CaCO_3$ toward contaminant ions simulated by molecular dynamics (MD). (d) Number density profiles of contaminant ions along the Z-axis perpendicular to the $CaCO_3$ interface. (e) Adsorption energy at the interface, including van der Waals and electrostatic contributions. (f) Mean squared displacement (MSD) of contaminant ions, reflecting their mobility and binding strength.

aggregates. So next, we investigate the macro- and micro-performance of the resulting mortars.

3.2. *Performance of $CaCO_3$@IBA in mortars*

3.2.1. *Mechanical strength*

The mechanical strength properties of mortars incorporating 10 wt% and 30 wt% of sand replacement with both IBA and $CaCO_3$@IBA are investigated, and the results are presented in Fig. 7.

Compressive strength and its development trend of different mortars are illustrated in Fig. 7a and b. Mortars with pure sand (PSM) exhibited the highest compressive strength at all curing ages (3, 7, and 28 d), while the strength decreased as the substitution level of both aggregates increased. The overall reduction is significant, ranging from 16% to 36%. This is primarily attributed to the inferior mechanical properties of IBA-based aggregates compared to natural sand, which compromises the load-bearing capacity of the mortar matrix, especially at higher substitution levels [78]. Among these, the 28-d compressive strengths of mortars with $CaCO_3$@IBA were higher than those of mortars with the IBA, showing an increase of 11.35% at a 10% replacement level and 16.29% at a 30% replacement level. This phenomenon can be attributed to several factors. Firstly, the CC treatment immobilizes heavy metal ions in the IBA, thereby minimizing their adverse effects on cement hydration. Secondly, the newly formed $CaCO_3$ phases not only fill the internal pores of the IBA structure, enhancing its strength, but also act as heterogeneous nucleation sites that accelerate cement hydration reaction. Finally, the early-stage carbonation process oxidizes part of the metallic Al in the bottom ash, mitigating expansion caused by the metallic Al swelling reaction and improving the structural stability of the corresponding mortars. The smallest drop of 16% was observed in the mortar with 10% replacement using $CaCO_3$@IBA. While the strength increases with curing time, the growth rate slows down (Fig. 7b). At 3 days, compressive strengths of mortars with substitutions of both aggregates showed around 85% of their 28-day compressive strength, higher than the 80% observed in PSM. However, the overall growing rate of strength development was lower in mortars with both aggregate substitutions than in PSM. This is mainly due to the limited continuation of hydration reactions, hindered by the metallic swelling reaction between residual aluminium in the bottom ash and alkaline cement matrix [79].

The flexural strength and its development trend are exhibited in Fig. 7c and d. At 28 days, the variation of the flexural strength of the mortar is similar to compressive strength, lower than that of control mortars, and the total decrease is smaller than that of the compressive strength. Exceptionally, the CIBAM10 achieves the largest flexural strength of 7.22 MPa at 28-day curing, which is higher than that of PSM. This may result from the pozzolanic reaction between the IBA-based aggregates and cement, generating more hydration products (e.g., C-S-

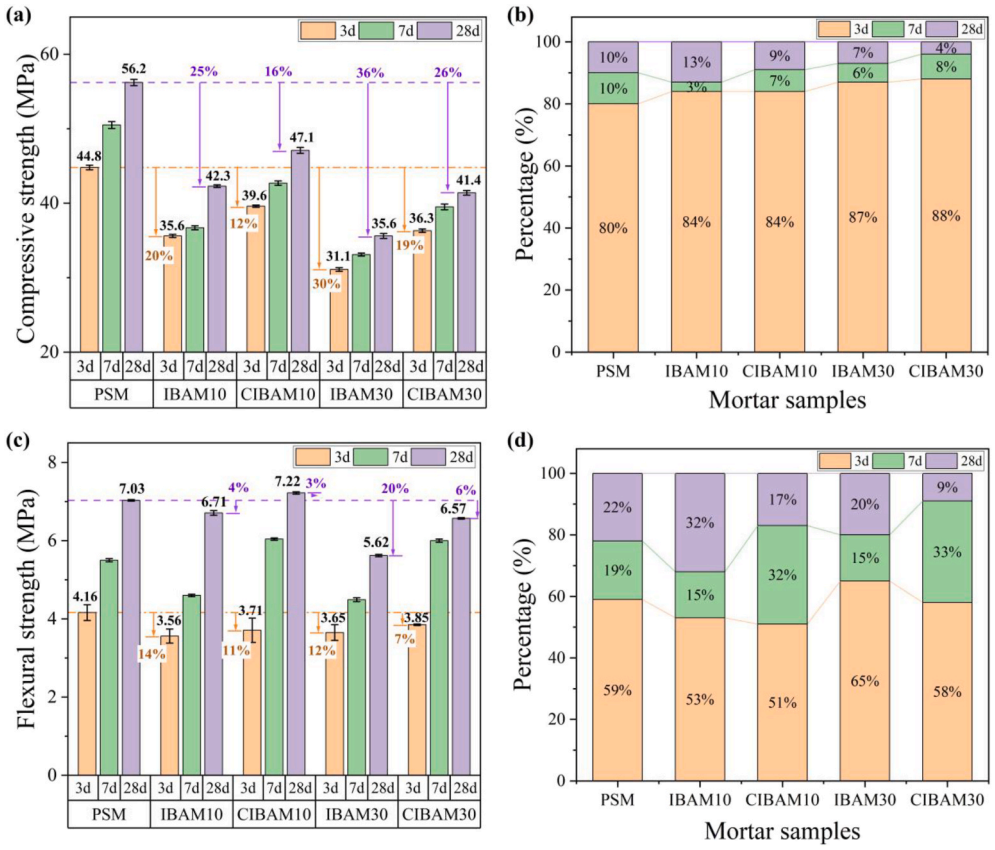

Fig. 7. Mechanical strength of different mortars: (a) compressive strength, (b) corresponding development trend of compressive strength; (c) flexural strength, (d) corresponding development trend of flexural strength.

H gel) to improve the flexural strength of the mortars [80]. At 3 days of curing, the flexural strength of IBAM10, CIBAM10, IBAM30, and CIBAM30 mortar specimens were 14%, 11%, 12%, and 7% lower, respectively, than that of PSM. However, similar to the compressive strength findings, mortar with $CaCO_3$@IBA consistently outperformed those with the IBA at the same substation level, with flexural strength increases of 7.6% and 16.9% at 10% and 30% replacement levels, respectively. These results can well confirm the positive effect of CC

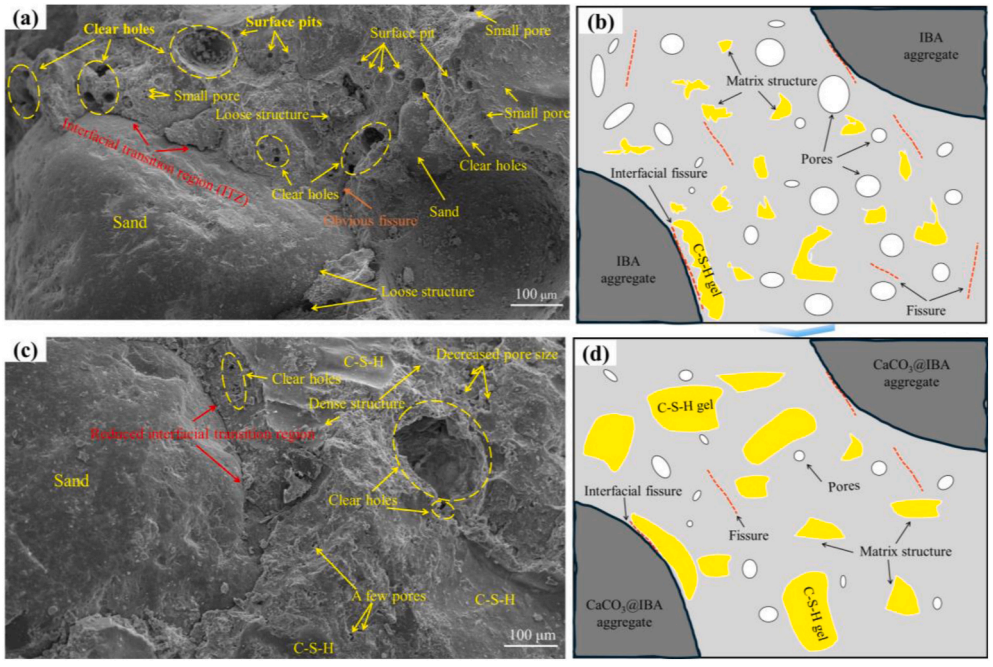

Fig. 8. Microstructures of different mortars with IBA and $CaCO_3$@IBA: (a) IBAM10, corresponding mechanism illustration (b); (c) CIBAM10, corresponding mechanism illustration (d).

treatment on the mechanical strength performance of mortars with the IBA.

3.2.2. Microstructure analysis

The macroscopic strength characteristics are largely governed by the microstructure properties. Mortar specimens are composite systems consisting of the cement matrix, IBA/$CaCO_3$@IBA aggregates, and the interfacial transition zone (ITZ). Thus, these microstructural systems of mortars with IBA and $CaCO_3$@IBAs under all substitution levels were investigated after load-bearing cracks. Fig. 8 presents the microstructural characteristics of typical mortar specimens (IBAM10 and CIBAM10) after impact loading and the corresponding mechanism illustration. For the remaining mortar specimens at a 30% substitution level (IBAM30 and CIBAM30), the microstructural characteristics and related mechanism illustrations are displayed in the supplementary information (Fig. S4). In addition, the Si/Ca, Al/Ca, and Al/Si molar ratios of the mortar matrices were calculated based on EDS measurements performed on four randomly selected matrix regions for each specimen. The results are summarized in Table S8.

As shown in Fig. 8a, the microstructures of the matrix of IBAM10 were relatively loose, with visible and deep pores and numerous surface pits. In contrast, the mortar specimen with $CaCO_3$@IBA (Fig. 8c) exhibited a dense matrix structure with the surface nearly free of pits and pores, though a few pores remained. A reduced number of fissures was also observed. Similar and more visible changes were also found in mortar specimens (IBAM30 and CIBAM30, Fig. S4). To noticeably compare microstructural changes that occur because of adding IBA and $CaCO_3$@IBA to the cement matrix, the broken cross-section images were schematically illustrated (Fig. 8b and d). Compared to the matrix of IBAM10, CIBAM10 exhibits a visibly reduced pore size and pore volume, indicating a more compact microstructure. A higher amount of hydration products, particularly C-S-H gel, is generated, as supported by the relatively elevated Si/Ca molar ratio (approximately 0.4) [81]. In addition, the interfacial transition zone (ITZ) between the cementitious matrix and aggregates appears significantly refined in CIBAM10. These microstructural improvements can be attributed to the CC treatment, which mitigates the swelling reaction of residual metallic aluminium in IBA. This mechanism is supported by the lower Al/Si molar ratio measured in CIBAM10 compared with IBAM10 (Table S8), indicating reduced aluminium-related reactions. The suppression of aluminium-induced expansion is primarily associated with a decrease in pH and the prevention of alkaline substances from the cement matrix migrating into the IBA structure. Moreover, newly formed nano-sized $CaCO_3$ accelerates the cement hydration process and the formation of calcium-silicate-hydrate (C-S-H) gels through nucleation and chemical reaction, which improves mechanical strength. This explanation is also confirmed by previous studies [82–84].

To further understand the pore characteristics of the microstructure, Brunauer-Emmett-Teller (BET) surface area analysis was conducted on mortar specimens incorporating the IBA and $CaCO_3$@IBA aggregates. As BET analysis is mainly sensitive to micro- and mesoporous structures, it does not capture capillary or macropores in cement-based systems. Accordingly, the BET technique was employed to evaluate fine-scale pore refinement and matrix densification, rather than to provide a comprehensive pore size distribution. The N_2 adsorption-desorption isotherm and corresponding pore size distributions from the BET test are given in Fig. 9, and the detailed BET analysis results are listed in Table 4. According to the pore classification defined by IUPAC [85], the pore structure of the mortar specimens containing the IBA-based aggregates can correspond to the type V isotherm. The results indicate that

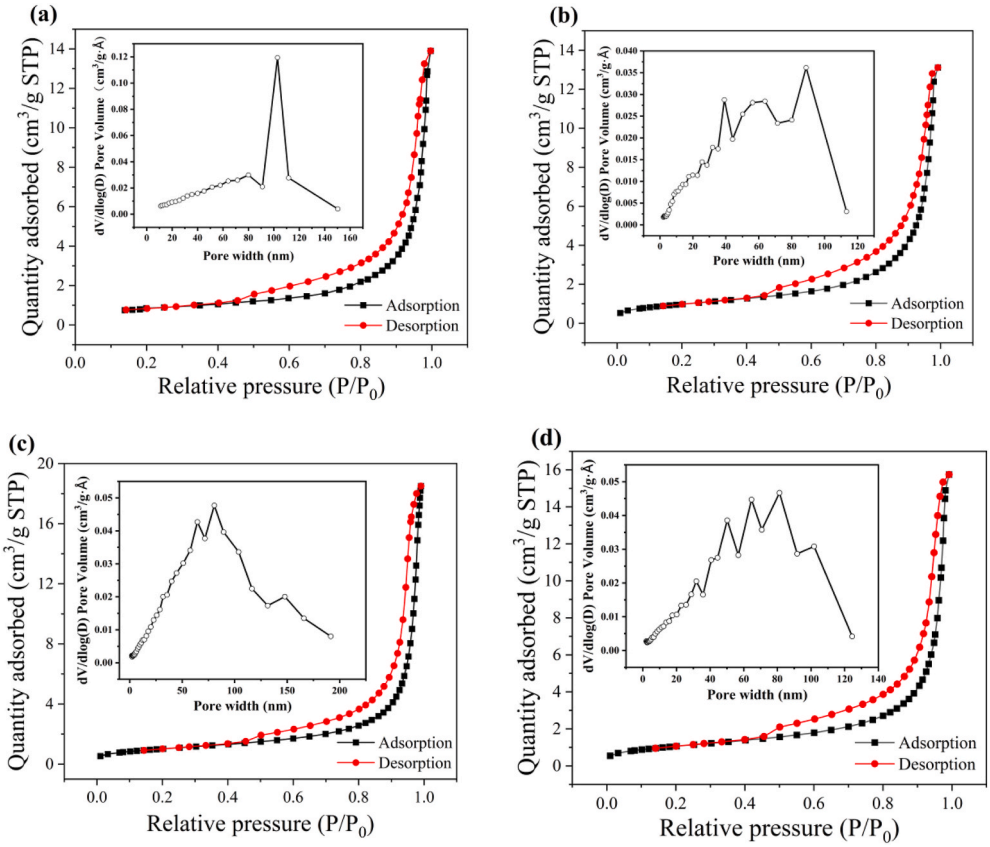

Fig. 9. BET analysis results of different mortars containing the IBA and $CaCO_3$@IBA aggregates: N_2-adsorption-desorption isotherm plots of (a) IBAM10; (b) CIBAM10; (c) IBAM30; and (d) CIBAM30. The inset represents the pore size distribution results calculated from the BJH desorption pore volume data for the respective specimens.

Table 4
Surface area and pore size of different mortar specimens.

Microstructure properties	IBAM10	CIBAM10	IBAM30	CIBAM30
BET surface area (m^2/g)	3.03	3.57	3.73	3.92
Micropore volume (cm^3/g)	0.000037	0.000079	0.000096	0.000133
Average pore size (nm)	25.83	20.39	27.52	24.94

the adsorption volume of mortars with $CaCO_3$@IBA evidently decreases compared to those with the IBA. For example, at a 10% replacement level, the IBAM10 specimen exhibits an adsorbed volume of about 14 cm^3g^{-1} STP, whereas the CIBAM10 specimen shows a lower volume of around 13 cm^3g^{-1} STP. This reduction is due to the CC treatment of the IBA, which can mitigate the metallic aluminium swelling reaction, linked to reduced pore size and amount of the mortar matrix. These findings are consistent with the SEM observation.

According to Table 4, similarly, the BET test reveals distinct results for average pore size in different mortars labelled IBAM10, CIBAM10, IBAM30, and CIBAM30. The mortar specimens have pore sizes of 25.83 nm, 20.39 nm, 27.52 nm, and 24.94 nm, respectively. The average pore size of mortars containing $CaCO_3$@IBA at replacement ratios of 10% and 30% are decreased by 21.05% and 9.38%, respectively, compared to those with the IBA. This suggests the decrease of the swelling reaction caused by metal aluminium in an alkaline matrix environment. In contrast, CIBAM10 and CIBAM30 exhibit increased BET surface area and micropore volume compared to their counterparts. The observed behaviour can be explained by increased C-S-H gel generation in the presence of $CaCO_3$@IBA, which leads to the development of additional micropores. The CC treatment increases $CaCO_3$ content, which in turn promotes the generation of C-S-H gel through both heterogeneous nucleation and chemical reactions.

In summary, the microstructural observations and BET analysis of mortars with both IBA aggregates correlated well with the mechanical strength difference. The CC treatment of the IBA can optimize the pore structure, improving the strength properties of the resulting mortar specimens. Nevertheless, such microstructural modifications will likely

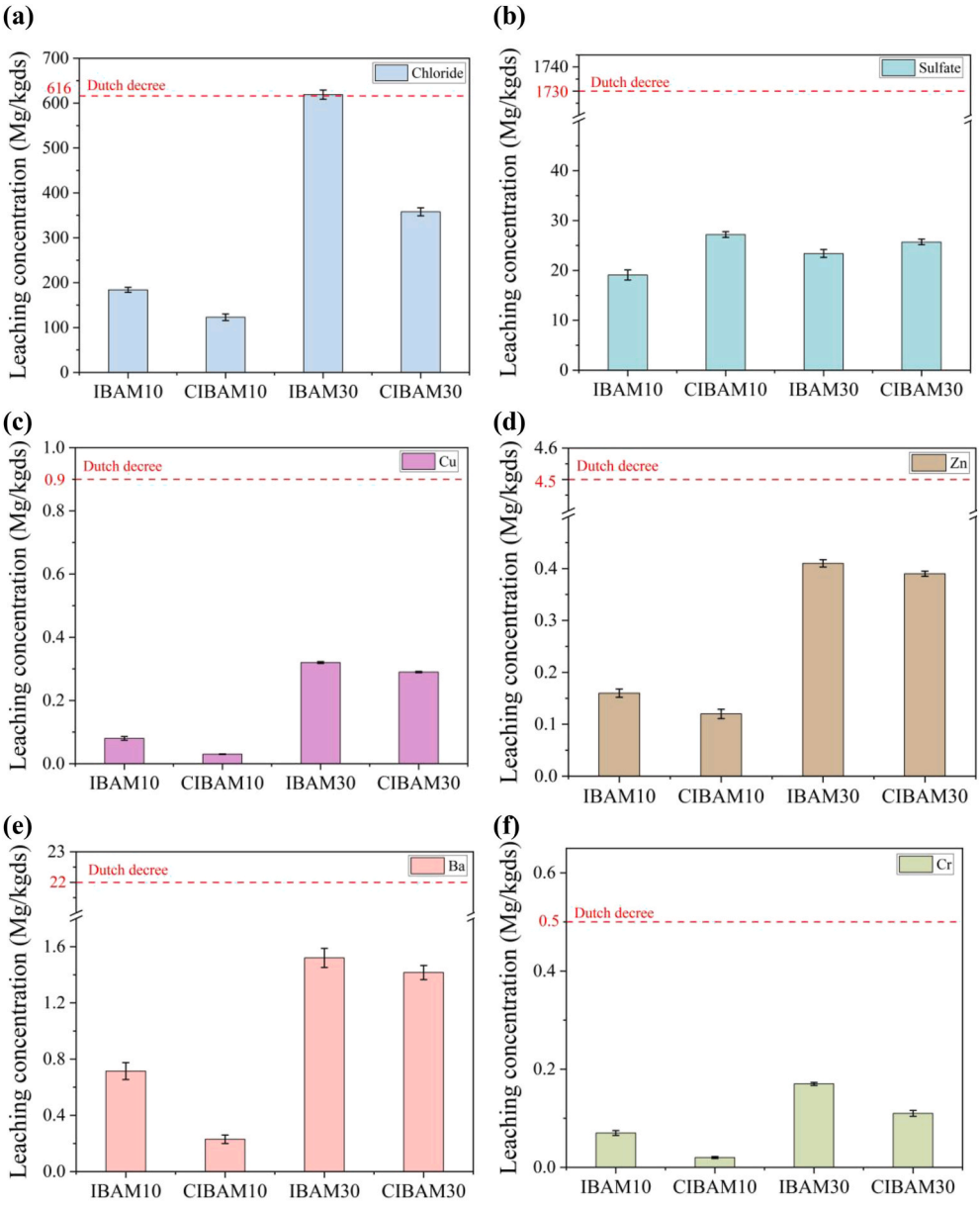

Fig. 10. The leachate concentration of different toxic elements (a, Chloride; b, Sulfate; c, Cu; d, Zn; e, Ba; and f, Cr) in the broken mortars containing the IBA and $CaCO_3$@IBA aggregates according to the EN 12457-2 test and the SQD legal limit values.

affect the leaching behaviour of contaminant ions. So next, we specifically investigate the leaching characteristics of mortars incorporating the IBA and $CaCO_3$@IBA aggregates.

3.2.3. Leaching behaviour

According to the microstructure analysis of the cementitious matrix, the CC treatment applied to the IBA aggregates was shown to reduce the pore structure, densifying the matrix, thereby enhancing the immobilization of contaminants. Therefore, the effect of the IBA aggregates after CC treatment on the leaching behaviour of cement mortars incorporating different aggregate replacement levels was investigated to determine their safety and application potential. All leaching concentrations are expressed in mg/kgds, where ds denotes dry solid mass, to exclude the influence of moisture content. The concentration of Mo in all leachates was below the detection limit. Fig. 10 compares the results to the legal limits set in the Dutch Soil Quality Decree [86] by the Dutch government, As can be seen, the leaching concentrations of other toxic contaminants in the hardened mortars ranged from 0.03 to 0.32 mg/kg_{ds} for Cu, 0.12 to 0.41 mg/kg_{ds} for Zn, 123 to 591 mg/kg_{ds} for Cl, and 19.1 to 27.2 mg/kg_{ds} for SO_4, respectively. These values are substantially lower than those observed for IBA aggregates alone, owing to the effective immobilization of contaminant ions by cement hydration products such as calcium-silicate-hydrate gel and ettringite [71].

As observed, mortars incorporating $CaCO_3$@IBA exhibited significantly lower leaching concentrations of contaminant ions than those containing the IBA. Notably, although the leachate concentrations of chloride in mortars containing the IBA exceeded the corresponding Dutch legislative limits (Fig. 10a and e), the application of the CC treatment reduced these values to below the regulatory thresholds for unmould building materials. These results demonstrate that the CC treatment effectively mitigates the leaching potential of the IBA when used as a fine aggregate substitute in hardened mortars.

Comprehensively, the CC treatment applied to the IBA aggregates densifies the cementitious matrix microstructure, which not only enhances the mechanical performance of the resulting mortars but also effectively reduces the leaching behaviour of their aggregates and corresponding mortars. From a technical perspective, the CC treatment approach is a feasible approach for increasing the substitution level of the IBA as fine aggregates. To assess the future scalability of this CC technique, we investigate its economic feasibility and environmental impacts at an industrial scale in industrial up in subsequent sections.

3.3. Economic and environmental benefit evaluation

3.3.1. Scaling-up economic evaluations

Fig. 11a illustrates the discounted cash flow diagram for the recovery scheme over a 10-year operation period. The NPV, cumulative annual revenue, capital cost, and cumulative manufacturing cost were estimated based on the modes of the factors' triangle distributions. The designed process is projected to yield approximately 38400 tons of $CaCO_3$@IBA aggregates and 12700 tons of PCC annually. The total revenue from product sales over the entire project lifespan is estimated at €75 million. Based on the profitability analysis, the NPV at the end of the 10 years is estimated to be €47 million. The discounted payback period of the project is about 2.11 years following plant commissioning.

The distributions of NPV and BCR generated from the Monte Carlo

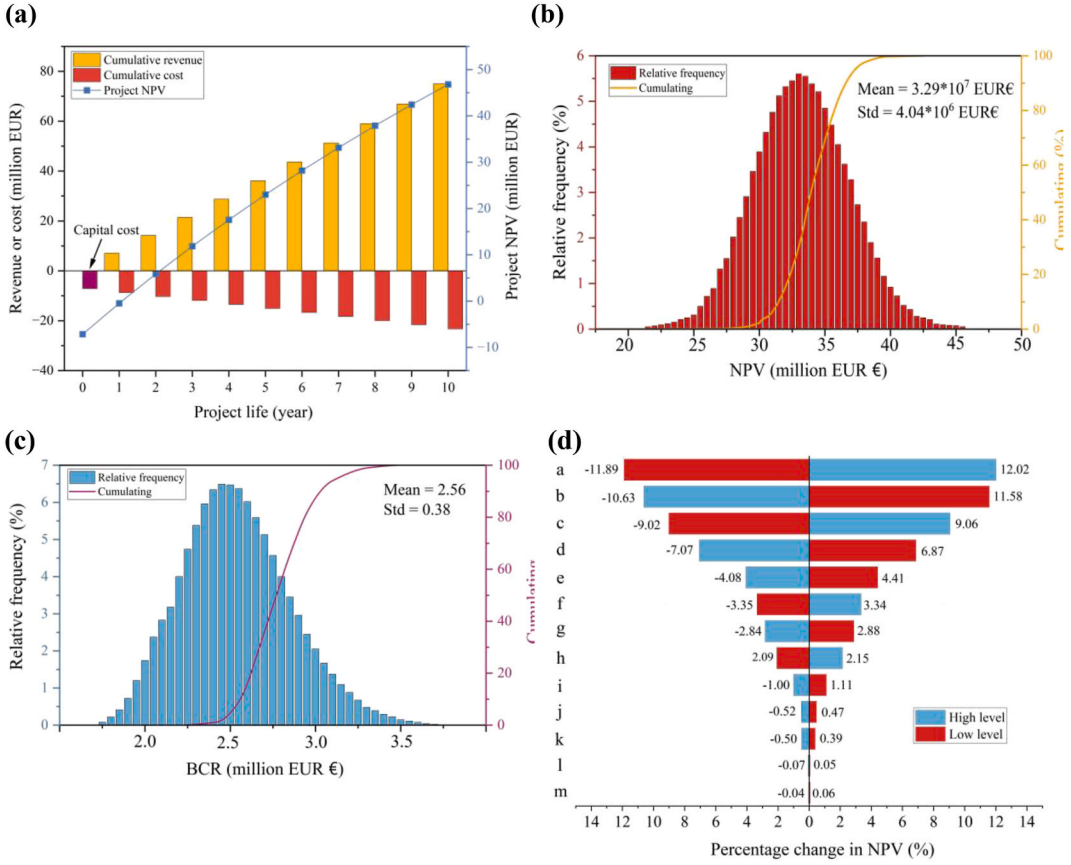

Fig. 11. Economic benefit panel. (a) Discounted cash flow diagram for the proposed process, including project net present value, cumulative annual revenue, cumulative capital cost, and cumulative manufacturing cost. (b) Distribution of Net Present Value, cumulative generated from Monte Carlo simulation. (c) Benefit Cost Ratio and cumulative generated from the Monte Carlo simulation. (d) Sensitivity analysis results for selected economic parameters: a, $CaCO_3$@IBA income; b, discount rate; c, PCC income; d, land cost; e, wastewater treatment cost; f, saved CO_2 tax; g, operating cost; h, saved gate fee & landfill tax; i, water cost; j, depreciation & maintenance cost; k, equipment cost; l, transportation cost; m, quicklime cost.

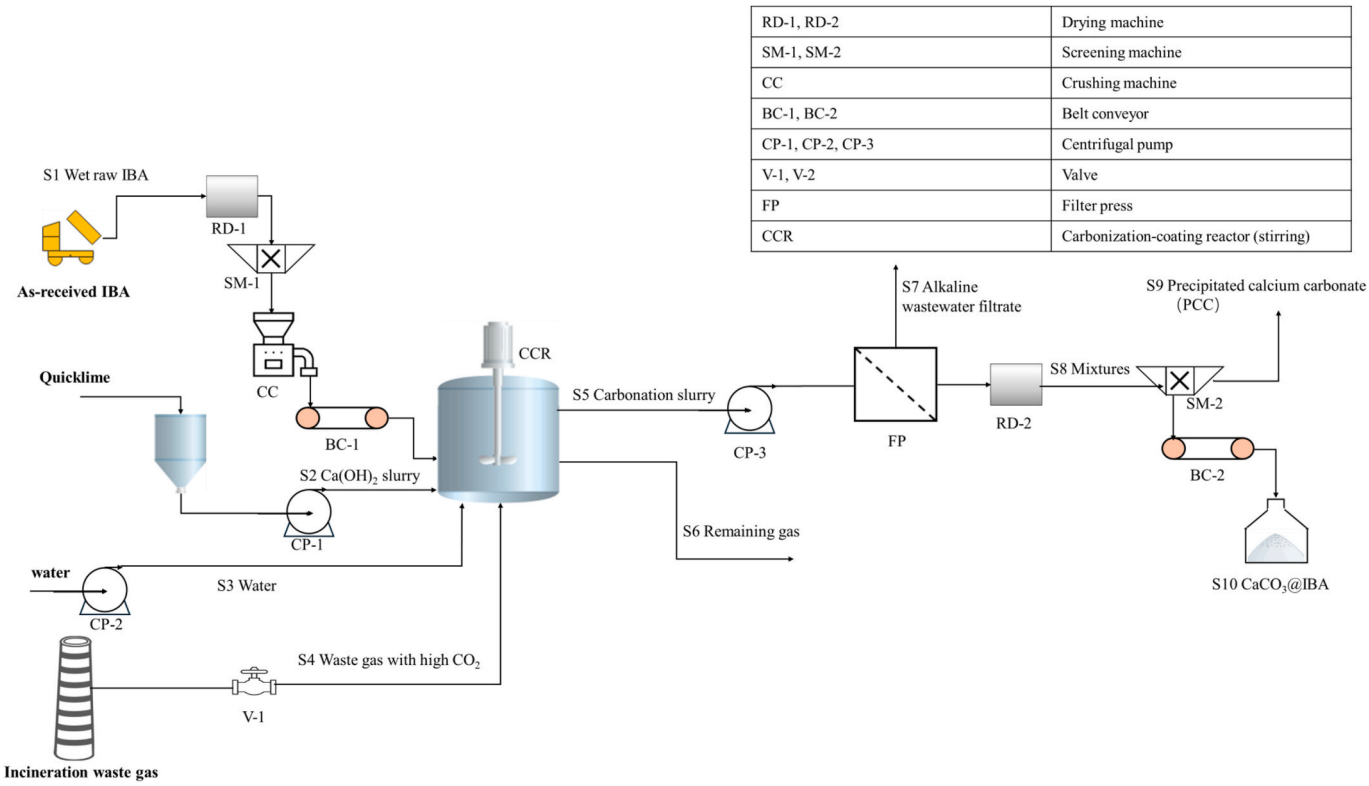

Fig. 12. Schematic illustration of the industrial pilot-scale process for the proposed IBA carbonation coating.

simulation are presented in Fig. 11b and c. For the proposed process, the average NPV over a 10-year operational period is estimated at €32.9 million. As shown in Fig. 11b, over 99% of NPV is positive, indicating that the proposed process is more than 99% of being economically viable. These results suggest strong potential for commercial-scale implementation of the CC treatment for the IBA derived from WtE plants. Similar to the NPV results, the relative frequency of positive BCR is more than 99%. The mean BCR is 2.56, indicating that the net profit is expected to be about 2.5 times the total investment, thus providing strong support for the economic feasibility of the industrial-scale CC process. Meanwhile, these BCR results further reinforce the conclusions drawn from NPV analysis. It is worth noting that the economic evaluation was conducted assuming a 10-year operational period. Extending the service life of the plant would likely result in higher NPV and BCR.

A sensitivity analysis was conducted to evaluate the impact of key economic parameters on the output NPV, as illustrated in Fig. 11d. The percentage changes in NPV were calculated by varying each selected parameter between the lower and upper bounds of its respective triangular distribution. Parameters (i.e., $CaCO_3$@IBA income, PCC income, saved CO_2 taxes, and saved gate fee & landfill tax exhibited a positive correlation with NPV, whereas other economic parameters showed a negative relationship. Among these, the income from $CaCO_3$@IBA was identified as the most sensitive parameter, resulting in an approx. 12% change in NPV when varied across its distribution range. This was followed by the discount rate, at around 11%. In contrast, transportation cost and quicklime cost were found to be the least sensitive parameters, which can be attributed to the relatively low transport frequency and the low unit price of raw quicklime.

3.3.2. *Environmental evaluation*

Based on the laboratory experimental results, the CC treatment not only effectively inhibited the contaminant ion leaching but also enabled the valorisation of the IBA and flue gas CO_2, thereby reducing net carbon emissions. These combined effects contribute to mineral resource sustainability and decarbonation. Therefore, the environmental impacts of the CC treatment at the industrial scale, with particular emphasis on greenhouse gas emissions, were further investigated to assess its significance and application potential (Fig. 13).

The environmental performance of producing 1 ton of sustainable $CaCO_3$@IBA aggregates was evaluated using eight environmental impact indicators, as illustrated in Fig. 13a. The net values for all eight categories were negative, indicating that the upscaled CC process provides overall environmental benefits by mitigating these impacts. Among these indicators, the most significant reductions were observed for TEP (1410 kg 1,4-DCB eq.), HTP (−505.7 kg 1,4-DCB eq.), and GWP (−30.8 kg CO_2 eq.). The TEP and HTP are primarily associated with the presence of toxic constituents in the IBA, whereas the GWP is mainly influenced by the utilization of incineration flue gas CO_2 and the concurrent reduction in natural sand extraction. To further elucidate the contributors to GWP, the carbon footprint transfer process is illustrated using a Sankey diagram (Fig. 13b). Among all process stages, the quicklime preparation stage represents the largest contributor to global warming, while the carbon footprints are ultimately transferred to the main product, $CaCO_3$@IBA, electricity consumption, and by-product PCC. In addition, the reduction in eight environmental indicators is primarily concentrated in the stage following the CC treatment (Fig. S5). A possible reason for this reduction is the absorption of CO_2 from incineration flue gas and the immobilization of toxic constituents during the CC process.

Furthermore, based on global WtE plant data (Table S5), the calculated reduction in GWP associated with the industrial-scale CC strategy was greater in China and the United States (Fig. 13c), primarily due to the higher demand for sustainable $CaCO_3$@IBA aggregates in the construction sector. Similarly, within the Netherlands, the North and South Holland provinces exhibited the highest GWP reduction potential (Table S6 and Fig. 13d), owing to the substantial potential for CC treatment associated with the relatively larger quantities of IBA generated compared with other provinces. These findings support the environmental sustainability of the IBA industrial-scale CC treatment, highlighting its potential to advance carbon neutrality and sustainable

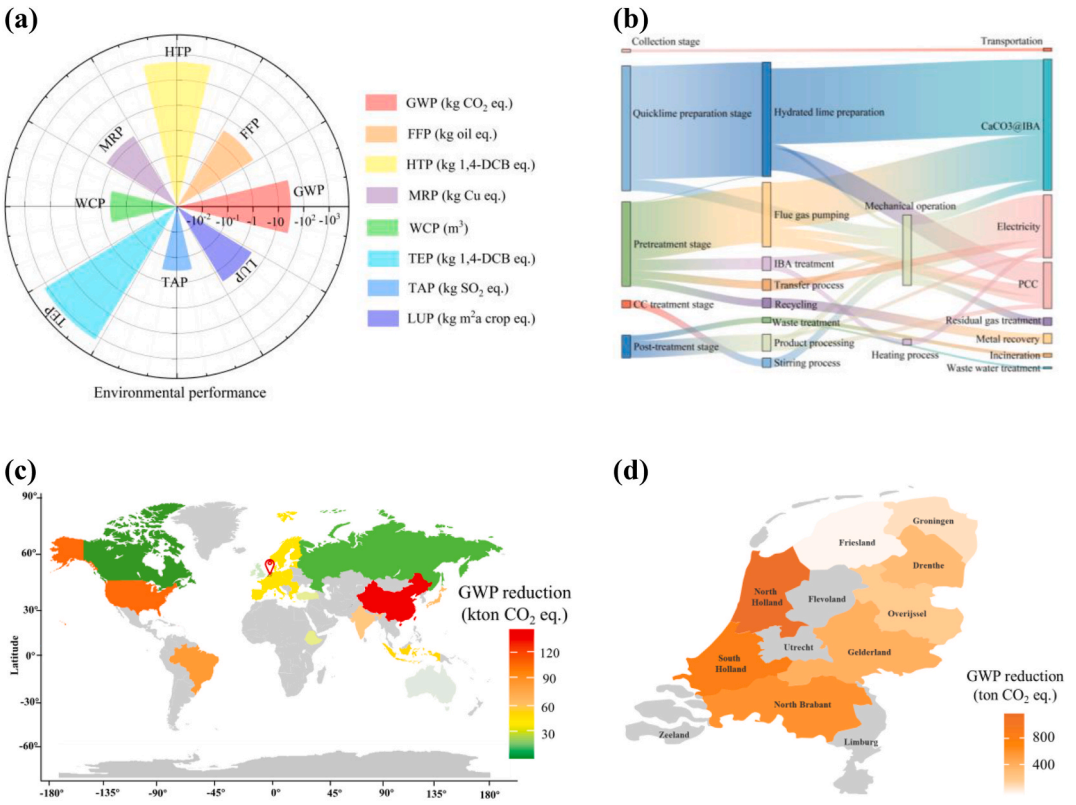

Fig. 13. Environmental impact assessment of industrial-produced $CaCO_3$@IBA aggregates. (a) Environmental across eight indicators for industrial scale carbonation treatment: global warming potential (GWP, kg CO_2-eq); fossil fuel potential (FFP, kg oil -eq); human toxicity potential (HTP, kg 1,4-DCB-eq); mineral resource potential (MRP, kg Cu eq); water consumption potential (WCP, m^3); terrestrial ecotoxicity potential (TEP, kg 1,4-DCB-eq); terrestrial acidification potential (TAP, kg SO_2 eq); land use potential (LUP, m2a crop eq). (b) Carbon footprint transfer process; (c) The GWP reduction across different countries/regions based on the IBA production data. (d) The GWP reduction of different provinces in the Netherlands.

resource management.

4. Conclusion

In summary, a novel $CaCO_3$@IBA core-shell structure was successfully prepared through a cost-effective and green CC treatment strategy with the simultaneous generation of high-value byproduct PCC, and systematically evaluated as fine aggregate sand substitutes in construction materials. The formation of the core-shell architecture was confirmed by XPS, SEM, TEM, EDS, and XRD characterizations, which revealed well-defined $CaCO_3$ crystals and cauliflower-like micro/nano-structure of shell layers. Modified surface coverage model results elucidated the mass-transfer-controlled reaction kinetics of the CC treatment within a gas–liquid–solid three-phase system. Notably, the introduction of the $CaCO_3$ shell significantly enhanced contaminant immobilization through multiple mechanisms, including physical encapsulation, insoluble carbonates, doping, and co-precipitation with $CaCO_3$ crystals, as reflected by ICP-MS and IC results. MD simulation results further demonstrate that the $CaCO_3$ interface facilitates strong absorption of contaminant ions, thereby reducing their mobility during the CC treatment process.

When incorporated into mortar composites, the $CaCO_3$@IBA aggregates imparted superior mechanical strength, reduced pore volume, denser matrices, and enhanced immobilization capacity, fulfilling the Dutch legislative limitation for unmould building materials. Moreover, the proposed industrial scale-up design exhibited huge economic benefits, reaching up to €32.9 million over 10 years of operating. Simultaneously, this pilot process significantly improved environmental performance indicators, particularly in terms of GWP-30.8 kg CO_2 eq./ton $CaCO_3$@IBA aggregates, especially in countries with a high density of WtE plants. This study provides new insight into the large-scale and sustainable utilization of IBA in construction through "green synthesis of $CaCO_3$@IBA from incineration residues and flue gas", which is of great significance for advancing the development of zero-carbon construction materials. This work has confirmed the feasibility of applying CC technology to IBA aggregates. However, the long-term mechanical performance and potential leaching risks associated with utilizing $CaCO_3$@IBA as a sand replacement in concrete require further investigation.

CRediT authorship contribution statement

Helong Song: Writing – original draft, Methodology, Data curation. **Zhihan Jiang:** Writing – review & editing. **Theun S. Luinenburg:** Methodology. **Florent Gauvin:** Supervision. **Xiaowen Fu:** Methodology. **Xiaohui Sun:** Writing – review & editing, Formal analysis. **Zijun Dong:** Formal analysis. **Feng Wang:** Formal analysis. **Huiming Fan:** Visualization, Formal analysis. **Xiangsheng Chen:** Resources, Formal analysis. **H.J.H. Brouwers:** Visualization, Resources.

Declaration of competing interest

The authors declare that they have no known competing financial interests or personal relationships that could have appeared to influence the work reported in this paper.

Acknowledge

This research is supported by the National Natural Science Foundation of China (Grant No. 52500171), National Natural Science Foundation of China Excellent Young Scientists Fund (Grant No. 52422004),

Guangdong Basic and Applied Basic Research Foundation (No. 2026A1515012027) and 868/the Third Phase of High-Level University Construction (NO.000001033378), the College of Civil and Transportation Engineering of Shenzhen University (China), Key Laboratory of Coastal Urban Soil-Water Environmental Evolution, Ministry of Ecology and Environment (under construction) of Shenzhen University (China) and the Department of the Built Environment of Eindhoven University of Technology (the Netherlands). The authors thank Dipl. Min. K. Schollbach for help on the supply of MSWI bottom ash.

Appendix A. Supplementary data

Supplementary data to this article can be found online at https://doi.org/10.1016/j.cemconcomp.2026.106596.

Data availability

Data will be made available on request.

References

[1] L. Chen, L. Wang, D.-W. Cho, D.C. Tsang, L. Tong, Y. Zhou, J. Yang, Q. Hu, C. S. Poon, Sustainable stabilization/solidification of municipal solid waste incinerator fly ash by incorporation of green materials, J. Clean. Prod. 222 (2019) 335–343.
[2] R. Cremiato, M.L. Mastellone, C. Tagliaferri, L. Zaccariello, P. Lettieri, Environmental impact of municipal solid waste management using life cycle assessment: the effect of anaerobic digestion, materials recovery and secondary fuels production, Renew. Energy 124 (2018) 180–188.
[3] World Bank, Trends in Solid Waste Management, 2020. https://datatopics.worldbank.org/what-a-waste/trends_in_solid_waste_management.html. (Accessed 1 June 2025).
[4] W.-J. Long, J.-k. Peng, Y.-c. Gu, J.-l. Li, B. Dong, F. Xing, Y. Fang, Recycled use of municipal solid waste incinerator fly ash and ferronickel slag for eco-friendly mortar through geopolymer technology, J. Clean. Prod. 307 (2021) 127281.
[5] J. Ren, L. Hu, Z. Dong, L. Tang, F. Xing, J. Liu, Effect of silica fume on the mechanical property and hydration characteristic of alkali-activated municipal solid waste incinerator (MSWI) fly ash, J. Clean. Prod. 295 (2021) 126317.
[6] B. Chen, P. Perumal, M. Illikainen, G. Ye, A review on the utilization of municipal solid waste incineration (MSWI) bottom ash as a mineral resource for construction materials, J. Build. Eng. 71 (2023) 106386.
[7] D. Blasenbauer, F. Huber, J. Lederer, M.J. Quina, D. Blanc-Biscarat, A. Bogush, E. Bontempi, J. Blondeau, J.M. Chimenos, H. Dahlbo, Legal situation and current practice of waste incineration bottom ash utilisation in Europe, Waste Manage. (Tucson, Ariz.) 102 (2020) 868–883.
[8] M. Šyc, F.G. Simon, J. Hykš, R. Braga, L. Biganzoli, G. Costa, V. Funari, M. Grosso, Metal recovery from incineration bottom ash: state-Of-the-art and recent developments, J. Hazard Mater. 393 (2020) 122433.
[9] Y. Wang, H. Shi, Q. Wang, H. Wang, Y. Sun, W. Li, R. Bian, Insights into the landfill leachate properties and bacterial structure succession resulting from the colandfilling of municipal solid waste and incineration bottom ash, Bioresour. Technol. 361 (2022) 127720.
[10] H. Song, T. Liu, F. Gauvin, H. Brouwers, Investigation of sisal fiber incorporation on engineering properties and sustainability of lightweight aggregates produced from municipal solid waste incinerated bottom ash, Constr. Build. Mater. 413 (2024) 134943.
[11] Q. Wang, H. Chu, F. Li, Incorporating incineration bottom ash in environmentally friendly ultra-high performance concrete: impact on mechanical properties, durability, and environmental benefits, Constr. Build. Mater. 481 (2025) 141640.
[12] Q. Wang, H. Chu, J. Jiang, B. Zhu, Enhancing mechanical performance and durability of high strength mortar with incineration bottom ash via Al2O3 micro-powder: an experimental study, J. Build. Eng. 89 (2024) 109268.
[13] D. Bansal, G. Ramana, M. Datta, Sustainable utilization of incineration bottom ash in pavement construction: environmental impacts and life cycle assessment, Sci. Total Environ. 931 (2024) 172890.
[14] H. Chu, Q. Wang, W. Zhang, Optimizing ecological ultra-high performance concrete prepared with incineration bottom ash: utilization of Al2O3 micro powder for improved mechanical properties and durability, Constr. Build. Mater. 426 (2024) 136152.
[15] H. Li, H. Chu, Q. Wang, J. Tang, Feasibility of producing eco-friendly self-compacting mortar with municipal solid waste incineration bottom ash: a preliminary study, Case Stud. Constr. Mater. 19 (2023) e02309.
[16] Q. Wang, H. Chu, W. Shi, J. Jiang, F. Wang, Feasibility of preparing self-compacting mortar via municipal solid waste incineration bottom ash: an experimental study, Arch. Civ. Mech. Eng. 23 (4) (2023) 251.
[17] B. Verbinnen, P. Billen, J. Van Caneghem, C. Vandecasteele, Recycling of MSWI bottom ash: a review of chemical barriers, engineering applications and treatment technologies, Waste Biomass Valoriz. 8 (2017) 1453–1466.
[18] Y. Cheng, G. Gao, L. Chen, W. Du, W. Mu, Y. Yan, H. Sun, Physical and mechanical study of municipal solid waste incineration (MSWI) bottom ash with different particle size distribution, Constr. Build. Mater. 416 (2024) 135137.
[19] J. Bawab, J. Khatib, S. Kenai, M. Sonebi, A review on cementitious materials including municipal solid waste incineration bottom ash (MSWI-BA) as aggregates, Buildings 11 (5) (2021) 179.
[20] B. Chen, Y. Zuo, S. Zhang, L.M. de Lima Junior, X. Liang, Y. Chen, M.B. van Zijl, G. Ye, Reactivity and leaching potential of municipal solid waste incineration (MSWI) bottom ash as supplementary cementitious material and precursor for alkali-activated materials, Constr. Build. Mater. 409 (2023) 133890.
[21] P. Rożek, M. Król, A. Knapik, W. Mozgawa, Disposal of bottom ash from the incineration of hazardous waste in two different mineral matrixes, Environ. Prog. Sustain. Energy 36 (4) (2017) 1074–1082.
[22] E. Loginova, K. Schollbach, M. Proskurnin, H.J.H. Brouwers, Municipal solid waste incineration bottom ash fines: transformation into a minor additional constituent for cements, Resour. Conserv. Recycl. 166 (2021) 105354.
[23] X. Sun, Y. Yi, pH evolution during water washing of incineration bottom ash and its effect on removal of heavy metals, Waste Manag. 104 (2020) 213–219.
[24] K.A. Clavier, J.M. Paris, C.C. Ferraro, E.T. Bueno, C.M. Tibbetts, T.G. Townsend, Washed waste incineration bottom ash as a raw ingredient in cement production: implications for lab-scale clinker behavior, Resour. Conserv. Recycl. 169 (2021) 105513.
[25] X. Sun, Y. Yi, Acid washing of incineration bottom ash of municipal solid waste: effects of pH on removal and leaching of heavy metals, Waste Manag. 120 (2021) 183–192.
[26] Z. Chen, J.-S. Li, D. Xuan, C.S. Poon, X. Huang, Effect of alkaline washing treatment on leaching behavior of municipal solid waste incineration bottom ash, Environ. Sci. Pollut. Control Ser. 30 (1) (2023) 1966–1978.
[27] J. Xiang, J. Qiu, Z. Li, J. Chen, Y. Song, Eco-friendly treatment for MSWI bottom ash applied to supplementary cementing: mechanical properties and heavy metal leaching concentration evaluation, Constr. Build. Mater. 327 (2022) 127012.
[28] V. Caprai, K. Schollbach, M. Florea, H. Brouwers, Investigation of the hydrothermal treatment for maximizing the MSWI bottom ash content in fine lightweight aggregates, Constr. Build. Mater. 230 (2020) 116947.
[29] V. Caprai, K. Schollbach, H.J.H. Brouwers, Influence of hydrothermal treatment on the mechanical and environmental performances of mortars including MSWI bottom ash, Waste Manag. 78 (2018) 639–648.
[30] T. Astrup, Pretreatment and utilization of waste incineration bottom ashes: danish experiences, Waste Manage. (Tucson, Ariz.) 27 (10) (2007) 1452–1457.
[31] D. Blanc, L. Gonzalez, M. Lupsea-Toader, C. de Brauer, Mineralogical evolution and leaching behaviour of a heap of bottom ash as a function of time: influence on its valorization, Waste Biomass Valoriz. 9 (2018) 2517–2527.
[32] Y. Sun, B. Chen, S. Zhang, K. Blom, M. Luković, G. Ye, Characterization, pre-treatment, and potential applications of fine MSWI bottom ash as a supplementary cementitious material, Constr. Build. Mater. 421 (2024) 135769.
[33] G. Zhang, X. Luo, S. Li, L. Deng, Y. Liu, Z. Wang, Z. Li, M. Li, C. Xu, Interface characterization of ground anchors embedded in soybean urease-induced carbonate precipitation-stabilized soils, Acta Geotech (2026) 1–18.
[34] Z. Yao, A.K. Prabhakar, B.C. Mohan, C.-H. Wang, An innovative accelerated carbonation process for treatment of incineration bottom ash and biogas upgrading, Waste Manage. (Tucson, Ariz.) 144 (2022) 203–209.
[35] J. Liu, G. Liu, W. Zhang, Z. Li, H. Jin, F. Xing, A new approach to CO2 capture and sequestration: a novel carbon capture artificial aggregates made from biochar and municipal waste incineration bottom ash, Constr. Build. Mater. 398 (2023) 132472.
[36] L. Cheng, H. Jin, Y. Wu, Y. Ren, J. Liu, F. Xing, Influence of municipal solid waste incineration bottom ash particle size on cement hydration and performance, Constr. Build. Mater. 432 (2024) 136516.
[37] F.B. Brück, Accelerated Carbonation of Waste Incinerator Bottom Ash for Trace Metal Immobilisation, Universität zu Köln, 2019.
[38] E. Rendek, G. Ducom, P. Germain, Carbon dioxide sequestration in municipal solid waste incinerator (MSWI) bottom ash, J. Hazard. Mater. 128 (1) (2006) 73–79.
[39] N.M. Alderete, A.M. Joseph, P. Van den Heede, S. Matthys, N. De Belie, Effective and sustainable use of municipal solid waste incineration bottom ash in concrete regarding strength and durability, Resour. Conserv. Recycl. 167 (2021) 105356.
[40] Y.-F. Yang, G.-S. Gai, S.-M. Fan, Surface nano-structured particles and characterization, Int. J. Miner. Process. 78 (2) (2006) 78–84.
[41] H. Fan, H. Song, X. Wang, D. Gao, G. Zhu, Y. Qi, J. Liu, Effect of the formulation control agent on brightness of modified fly ash and its potential application in papermaking, Bioresources 13 (2) (2018) 3462–3472.
[42] H. Fan, H. Song, Y. Rao, X. Wang, G. Zhu, Q. Wang, Y. Qi, G. Zhu, D. Gao, J. Liu, Effect of calcium hydroxide concentration and stirring rate on the crystallization of the calcium carbonate on the surface of fly ash, BioResources (2018).
[43] K. Schnabel, F. Brück, T. Mansfeldt, H. Weigand, Full-scale accelerated carbonation of waste incinerator bottom ash under continuous-feed conditions, Waste Manage. (Tucson, Ariz.) 125 (2021) 40–48.
[44] R.J. Yeo, A. Sng, C. Wang, L. Tao, Q. Zhu, J. Bu, Strategies for heavy metals immobilization in municipal solid waste incineration bottom ash: a critical review, Rev. Environ. Sci. Biotechnol. 23 (2) (2024) 503–568.
[45] T. Suzuki, T. Kawai, Y. Kamijima, S. Shinohara, M. Tanaka, Application of ultrafine bubbles for enhanced carbonation of municipal solid waste incineration ash during direct aqueous carbonation, Sustainability 3 (2024) 100020.
[46] L. Cheng, H. Jin, W. Zhang, G. Xie, J. Liu, F. Xing, Influence of municipal solid waste incineration bottom ash on the hydration and carbonation behavior of reactive magnesia cement, Chem. Eng. J. 502 (2024) 158059.

[47] H. Fan, H. Song, Y. Rao, X. Wang, G. Zhu, Q. Wang, Y. Qi, G. Zhu, D. Gao, J. Liu, Effect of calcium hydroxide concentration and stirring rate on the crystallization of the calcium carbonate on the surface of fly ash, Bioresources 13 (3) (2018).
[48] P. Tang, M. Florea, P. Spiesz, H. Brouwers, Characteristics and application potential of municipal solid waste incineration (MSWI) bottom ashes from two waste-to-energy plants, Constr. Build. Mater. 83 (2015) 77–94.
[49] L.G. Joyner, E.P. Barrett, R. Skold, The determination of pore volume and area distributions in porous substances. II. Comparison between nitrogen isotherm and mercury porosimeter methods, J. Am. Chem. Soc. 73 (7) (1951) 3155–3158.
[50] E.C.f. Standardization, Methods of Testing Cement-Part 1, Determination of Strength, 2005.
[51] B.S. EN. 12457-2, characterisation of waste–leaching–compliance test for leaching of granular waste materials and sludges, British Standard, UK, 2002, https://doi.org/10.3403/BSEN12457.
[52] Y. Li, T. Han, M. Zhao, J. Han, R. Zhao, Z. Xu, W. Cao, M. Ma, C. Zhang, J. Luo, Modulating interfacial shear of nanoconfined hydration layer via surface charging, Nano Energy (2026) 111692.
[53] J.J.P.J. Bevers, The Dutch Carbon Dioxide Emission Tax, 2020. https://www.dentons.com/en/insights/alerts/2020/november/26/the-dutch-carbon-emission-tax.
[54] G. Zhan, Z. Yao, W.C. Ng, H. Li, M.X. Lim, Y. Zhi, S.N. Koh, C.-H. Wang, Economic production of monoclinic bismuth vanadate from waste vanadium ions: process design and cost-benefit analysis, J. Clean. Prod. 240 (2019) 118188.
[55] Lumivero, Powerful risk analysis for confident decision-making. https://lumivero.com/products/at-risk/, 2025. (Accessed 1 June 2025).
[56] PRé, SimaPro 9.4.0.1. https://pre-sustainability.com/, 2022.
[57] H. Song, F. Gauvin, T. Liu, X. Sun, Z. Dong, F. Wang, X. Chen, H.J.H. Brouwers, Understanding of municipal solid waste incineration (MSWI) bottom ash/cement blends: Impact of natural fiber on mechanical strength and leaching behavior, J. Build. Eng. (2026) 115330.
[58] ISO14040, Environmental Management: Life Cycle Assessment: Principles and Framework, 2006.
[59] ISO14044, Environmental management-life Cycle assessment-requirements and Guidelines, ISO, London, 2006.
[60] J. Xiao, L. Song, X. Guan, M. Bai, Mechanical, hydration process, and microstructural properties of eco-friendly UHDC incorporating recycled concrete powder, Constr. Build. Mater. 507 (2026) 145063.
[61] C.B. Whitehead, S. Özkar, R.G. Finke, LaMer's 1950 model for particle formation of instantaneous nucleation and diffusion-controlled growth: a historical look at the model's origins, assumptions, equations, and underlying sulfur sol formation kinetics data, Chem. Mater. 31 (18) (2019) 7116–7132.
[62] H. Song, K.C. Hon, F. Gauvin, S. Pantaleo, F. Berger, W. Chen, H. Brouwers, Durability assessment of alkyl ketene dimer hydrophobic treatment of bio-based thermal insulation materials, Resour. Conserv. Recycl. 212 (2025) 107983.
[63] A. Kiseler, V. Lygin, Infrared Spectra of Surface Compounds and Adsorbed Substances, Nauka, Moscow, 1992 (in Russian).
[64] W. Zhu, X. Chen, L.J. Struble, E.-H. Yang, Characterization of calcium-containing phases in alkali-activated municipal solid waste incineration bottom ash binder through chemical extraction and deconvoluted Fourier transform infrared spectra, J. Clean. Prod. 192 (2018) 782–789.
[65] G. Huang, Y. Ji, L. Zhang, J. Li, Z. Hou, Advances in understanding and analyzing the anti-diffusion behavior in complete carbonation zone of MSWI bottom ash-based alkali-activated concrete, Constr. Build. Mater. 186 (2018) 1072–1081.
[66] I.G. Lodeiro, D.E. Macphee, A. Palomo, A. Fernández-Jiménez, Effect of alkalis on fresh C–S–H gels. FTIR analysis, Cement Concr. Res. 39 (3) (2009) 147–153.
[67] Y. Sun, J.-s. Li, X. Chen, X. Huang, M. Guo, Y. Wan, L. Lu, Z. Chen, Z. Ma, Preparation and characteristics of modified red mud-municipal solid waste incineration bottom ash binder, J. Build. Eng. 46 (2022) 103760.
[68] M. Al-Ejji, M.K. Hassan, K. Youssef, F. Elmakaty, H. Mehanna, M. Sliem, M. Irshidat, Novel surface-treatment for bottom ash from municipal solid waste incineration to reduce the heavy metals leachability for a sustainable environment, J. Environ. Manag. 347 (2023).
[69] H. Cheng-Yong, L. Yun-Ming, M.M.A.B. Abdullah, K. Hussin, Thermal resistance variations of fly ash geopolymers: foaming responses, Sci. Rep. 7 (1) (2017) 45355.
[70] X. Sun, B. Xu, Y. Yi, Effects of accelerated carbonation on fine incineration bottom ash: CO_2 uptake, strength improvement, densification, and heavy metal immobilization, J. Clean. Prod. 475 (2024) 143714.
[71] T.-H. Su, H.-J. Yang, Y.-H. Shau, E. Takazawa, Y.-C. Lee, CO2 sequestration utilizing basic-oxygen furnace slag: controlling factors, reaction mechanisms and V–Cr concerns, J. Environ. Sci. 41 (2016) 99–111.
[72] R.M. Santos, J. Van Bouwel, E. Vandevelde, G. Mertens, J. Elsen, T. Van Gerven, Accelerated mineral carbonation of stainless steel slags for CO2 storage and waste valorization: effect of process parameters on geochemical properties, Int. J. Greenh. Gas Control 17 (2013) 32–45.
[73] C. Wei, J. Dong, H. Zhang, X. Wang, Kinetics model adaptability analysis of CO2 sequestration process utilizing steelmaking slag and cold-rolling wastewater, J. Hazard. Mater. 404 (2021) 124094.
[74] J. Qin, Y. Zhang, Y. Yi, M. Fang, Carbonation of municipal solid waste gasification fly ash: effects of pre-washing and treatment period on carbon capture and heavy metal immobilization, Environ. Pollut. 308 (2022) 119662.
[75] J. Chen, Y. Shen, Z. Chen, C. Fu, M. Li, T. Mao, R. Xu, X. Lin, X. Li, J. Yan, Accelerated carbonation of ball-milling modified MSWI fly ash: migration and stabilization of heavy metals, J. Environ. Chem. Eng. 11 (2) (2023) 109396.
[76] Y. Cheng, Z. Li, P. Zhang, J. Chen, C. Qin, CO2 mineralization and heavy metal leaching of multi-source ashes from municipal solid waste incineration, Sep. Purif. Technol. 354 (2025) 128825.
[77] B. Dash, B. Dash, S.S. Rath, A thorough understanding of the adsorption of Ni (II), Cd (II) and Zn (II) on goethite using experiments and molecular dynamics simulation, Sep. Purif. Technol. 240 (2020) 116649.
[78] K. Yan, H. Sun, F. Gao, D. Ge, L. You, Assessment and mechanism analysis of municipal solid waste incineration bottom ash as aggregate in cement stabilized macadam, J. Clean. Prod. 244 (2020) 118750.
[79] D. Xuan, P. Tang, C.S. Poon, Limitations and quality upgrading techniques for utilization of MSW incineration bottom ash in engineering applications–A review, Constr. Build. Mater. 190 (2018) 1091–1102.
[80] J. Yao, H. Song, Y. Li, Y. Cui, M. Chai, W. Ling, Mechanism of macro-and microscopic performance of cement mortars influenced by municipal solid waste incineration bottom ash as sand substitution, Constr. Build. Mater. 397 (2023) 132317.
[81] H. Song, T. Liu, F. Gauvin, H. Brouwers, Evaluation of zirconia modification on the durability of natural fiber-reinforced cement composites using accelerated aging, J. Build. Eng. 84 (2024) 108632.
[82] Q. Fu, Z. Zhang, X. Zhao, W. Xu, D. Niu, Effect of nano calcium carbonate on hydration characteristics and microstructure of cement-based materials: a review, J. Build. Eng. 50 (2022) 104220.
[83] D. Zhao, J.M. Williams, Z. Li, A.-H.A. Park, A. Radlińska, P. Hou, S. Kawashima, Hydration of cement pastes with calcium carbonate polymorphs, Cement Concr. Res. 173 (2023) 107270.
[84] B. Yang, Y. Li, H. Lin, W. Li, X. Liu, J. Shen, Study on crack resistance and impermeability of functional material modified concrete, Compos. Commun. (2026) 102703.
[85] M. Thommes, K. Kaneko, A.V. Neimark, J.P. Olivier, F. Rodriguez-Reinoso, J. Rouquerol, K.S. Sing, Physisorption of gases, with special reference to the evaluation of surface area and pore size distribution (IUPAC Technical Report), Pure Appl. Chem. 87 (9-10) (2015) 1051–1069.
[86] S.Q. Decree, Regeling Bodemkwaliteit, VROM, Ruimte En Milieu, Ministerie Van Volkshuisvesting, Ruimtelijke Ordeling En Milieubeheer, Den Haag, 2007.